MICROCOPY RESOLUTION TEST CHART
NATIONAL BUREAU OF STANDARDS 1963 A

CHEMICAL RESEARCH, —DEVELOPMENT & ENGINEERING CENTER

CRDEC-CR-88005

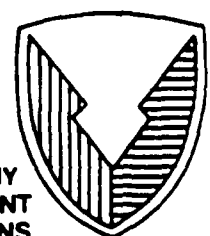# MULTIPLE SCATTERING FROM NONSPHERICAL TARGETS

by   Leonard D. Cohen
Richard D. Haracz
Ariel Cohen

DREXEL UNIVERSITY
Philadelphia, PA 19104

November 1987

DTIC
ELECTE
S **D**
JAN 0 6 1988

H

U.S. ARMY
ARMAMENT
MUNITIONS
CHEMICAL COMMAND

Aberdeen Proving Ground, Maryland 21010-5423

87

Disclaimer

The findings in this report are not to be construed as an official Department of the Army position unless so designated by other authorizing documents.

Distribution Statement

REPORT DOCUMENTATION PAGE

1a REPORT SECURITY CLASSIFICATION	1b RESTRICTIVE MARKINGS
UNCLASSIFIED	

2a SECURITY CLASSIFICATION AUTHORITY	3 DISTRIBUTION/AVAILABILITY OF REPORT
	Approved for public release; distribution
2b DECLASSIFICATION/DOWNGRADING SCHEDULE	is unlimited.

4 PERFORMING ORGANIZATION REPORT NUMBER(S)	5 MONITORING ORGANIZATION REPORT NUMBER(S)
CRDEC-CR-88005	Office of Naval Research

6a NAME OF PERFORMING ORGANIZATION	6b OFFICE SYMBOL (If applicable)	7a NAME OF MONITORING ORGANIZATION
Drexel University		Columbus, OH 43212-1194

6c. ADDRESS (City, State, and ZIP Code)	7b ADDRESS (City, State, and ZIP Code)
32d & Chestnut Streets Philadelphia, PA 19104	

8a. NAME OF FUNDING/SPONSORING ORGANIZATION	8b OFFICE SYMBOL (If applicable)	9 PROCUREMENT INSTRUMENT IDENTIFICATION NUMBER
CRDEC	SMCCR-RSP-B	DAAK11-84-0010

8c. ADDRESS (City, State, and ZIP Code)	10 SOURCE OF FUNDING NUMBERS			
	PROGRAM ELEMENT NO	PROJECT NO	TASK NO	WORK UNIT ACCESSION NO
Aberdeen Proving Ground, MD 21010-5423				

11 TITLE (Include Security Classification)

Multiple Scattering from Nonspherical Targets

12 PERSONAL AUTHOR(S)
Cohen, Leonard D., Haracz, Richard D., and Cohen, Ariel

13a TYPE OF REPORT	13b TIME COVERED	14 DATE OF REPORT (Year, Month, Day)	15 PAGE COUNT
Contractor	FROM 84 Jun TO 87 Jun	1987 November	63

16 SUPPLEMENTARY NOTATION
COR: Robert H. Frickel, SMCCR-RSP-B, (301) 671-3854

17	COSATI CODES		18 SUBJECT TERMS (Continue on reverse if necessary and identify by block number)
FIELD	GROUP	SUB-GROUP	Light scattering, Scattering by ellipsoids,
20	05		Scattering by cylinders, Scattering by helices,

19 ABSTRACT (Continue on reverse if necessary and identify by block number)

The Shifrin Acquista integral equation technique was modified to handle scattering from nonspherical, nonsymmetric particles, such as helices and toroids. This approach was applied to the analysis of an experiment on scattering by a helix with very good results. We also computed asymmetry factors for scattering from long cylinders. This result is useful in computing the average amount of light scattered in the forward direction from a collection of randomly oriented cylinders, such as a cloud of cylinders.

20 DISTRIBUTION/AVAILABILITY OF ABSTRACT	21 ABSTRACT SECURITY CLASSIFICATION
☒ UNCLASSIFIED/UNLIMITED ☐ SAME AS RPT ☐ DTIC USERS	UNCLASSIFIED

22a NAME OF RESPONSIBLE INDIVIDUAL	22b TELEPHONE (Include Area Code)	22c OFFICE SYMBOL
SANDRA J. JOHNSON	(301) 671-2914	SMCCR-SPS-T

PREFACE

The work described in this report was authorized under Contract No. DAAK11-84-0010. This work was started in June 1984 and completed in June 1987.

The use of trade names or manufacturers' names in this report does not constitute an official endorsement of any commercial products. This report may not be cited for purposes of advertisement.

Reproduction of this document in whole or in part is prohibited except with the permission of the Commander, U.S. Army Chemical Research, Development and Engineering Center, ATTN: SMCCR-SPS-T, Aberdeen Proving Ground, Maryland 21010-5423. However, the Defense Technical Information Center and the National Technical Information Service are authorized to reproduce the document for U.S. Government purposes.

This report has been approved for release to the public.

3

Blank

4

CONTENTS

Blank

MULTIPLE SCATTERING FROM NONSPHERICAL TARGETS

1. INTRODUCTION

In this report the development of a new extension of Shifrin's scheme for calculating the scattering by non-spherical, non-symmetric particles is documented and several applications presented. In addition we have developed a technique for properly computing the scattering of linearly polarized light by randomly oriented infinite cylinders, as well as finite cylinders and spheroids and we have applied this technique to several examples.

The new extension of Shifrin's method involves taking targets of arbitrary shape, but whose local cross section is circular, and breaking the target into a series of stacked disks. This particular approach permits the computation of scattering from such targets as helices, wavy cylinders, cylinders whose radii vary, and toroids, to cite a few. This new technique has been tested against an experiment conducted by Dr. Ru Wang of the University of Florida at Gainsville on scattering of microwave radiation by a dielectric helix. The comparison between the experiment and our calculated scattering patterns are included in this report and show good agreement.

We have also computed asymmetry factors for the scattering of polarized light from randomly oriented infinite cylinders. This problem required special care due to the peculiar scattering characteristics of very long cylinders. The results of this calculation are useful in computing the average amount of light scattered in the forward direction from a collection of randomly oriented cylinders such as a cloud of cylinders or randomly oriented fibers as used in insulation materials.

2. ASYMMETRY FACTORS FOR THE SCATTERING OF POLARIZED LIGHT FROM RANDOMLY ORIENTED INFINITE CYLINDERS

This computation is applicable to the scattering of light from fibrous media such as is used in construction and other applications. These fibers are characterized by a large aspect ratio (fiber length/ fiber diameter). We have recently shown[1,2] that for finite fibers with aspect ratios as small as 100, the theory for infinite cylinders gives highly accurate results. The second of the above references is a comparison between theory and an experiment.

In studying the passage of radiation through fibrous media, the main optical parameter is the ratio of the amount of radiative power scattered in the forward direction to the power scattered in all directions. In the case of spherical particles, this is called the asymmetry factor ρ, and for spheres larger than the wavelength of light (the size parameter $x = 2\pi a/\lambda$ is greater than unity) it is given by

$$\rho(x) = \int_0^1 I(\mu, x, m) \, d\mu \Big/ \int_{-1}^1 I(\mu, x, m) \, d\mu \; > 1/2 \tag{1}$$

where $\mu = \cos\theta$, with θ the scattering angle, and m is the refractive index.

For infinite cylinders, equation (1) must be modified to take into account the unique geometry for scattering from a sphere. Figure 1 shows this geometry, where the incident light is along the z axis, and the target axis is z_t. The scattered direction is z', and the direction of incident linear polarization
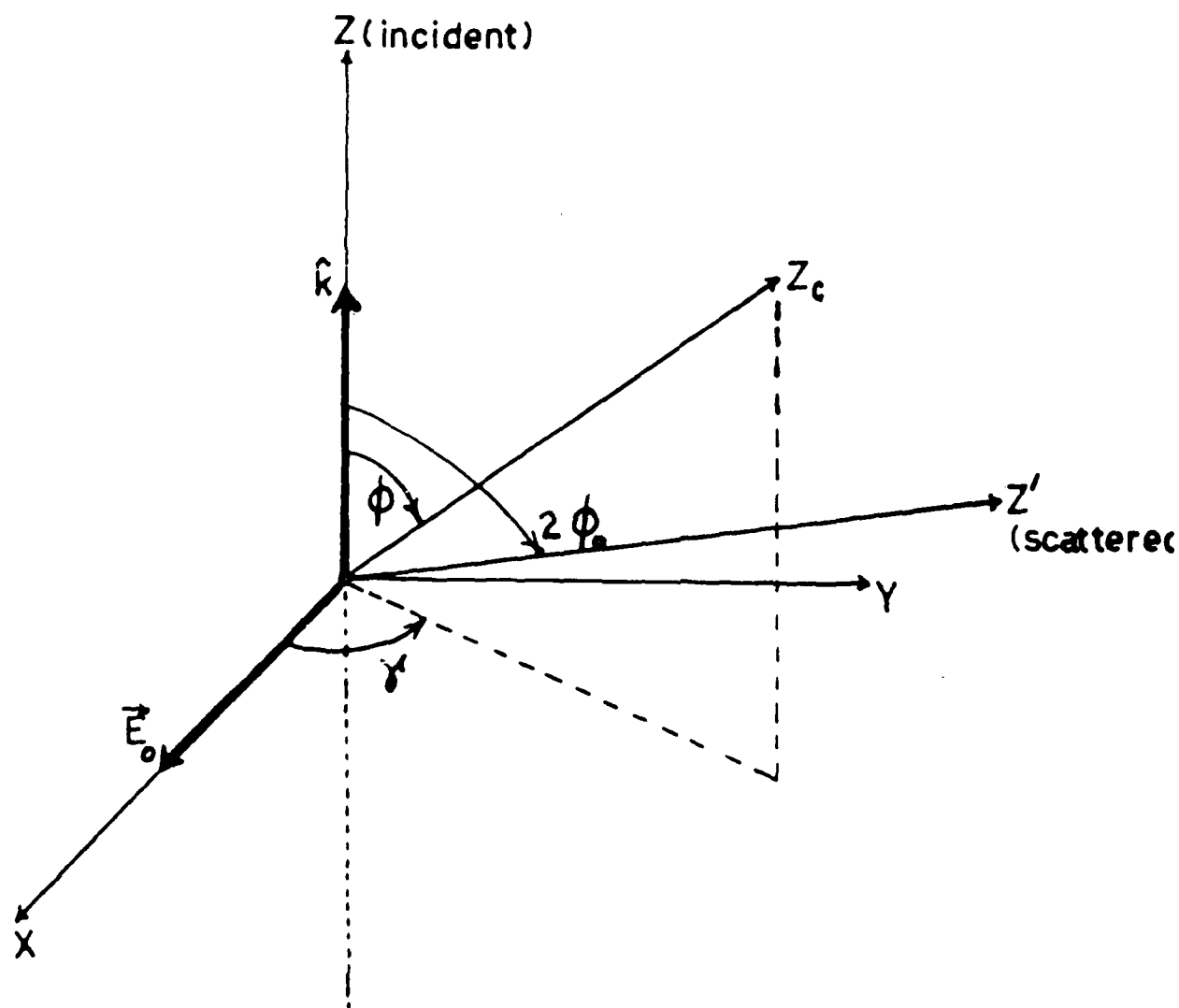
Figure 1. The geometry for the scattering process. The light is incident along the z axis and polarized along the x axis. The light is then scattered along the z' axis, and $2\phi_0$ is the angle between the incident and scattered directions. The cylinder axis is denoted z_c, and it s orientation angles with respect to xyz are θ (tilt angle) and γ (azimuthal angle).

8

defines the x axis. The scattering angle is denoted $2\phi_o$, and the orientation of the target axis is specified relative to xyz by the polar and azmuthal angles ϕ, γ .

For the scattering of light from an infinite cylinder, the scattering pattern is a cone with apex at the origin and symmetry axis along z' , as shown in figure 2. In this figure, the line OA is along the direction of incidence. Any other element of the cone is a possible scattering direction. For example, the direction OC is a scattered direction that is perpendicular to the direction of incidence. The point O' is at the center of the base of the cone, and the direction O'A is considered a reference for the measurement of a different kind of scattering angle - it is denoted θ , and it marks the angular distance from O'A to a point where a scattered direction line intersects the base of the cone. For example, the angle θ_C is the scattering angle for the scattered direction OC. It is shown [3,4] that the equation of constraint for infinite-cylinder scattering is given by

$$\sin \phi \sin \theta/2 \ = \sin \phi_o \tag{2}$$

The scattering angle θ for scattering in the plane perpendicular to the scattered direction is then given by ($\phi_o = 45°$)

$$\theta_A = \ |2 \sin^{-1} [1/\sqrt{2} \sin \phi] |. \tag{3}$$

We can now properly define the asymmetry factor for scattering from an infinite cylinder :

$$\rho(\phi,\gamma) = \int_{-\theta}^{\theta} (I_1 + I_2) \, d\theta \ / \ \int_{-\pi}^{\pi} (I_1 + I_2) \, d\theta . \tag{4}$$

In this equation I_1 and I_2 are the respective scattering intensities for the scattering of light respectively parallel and perpendicular to the scattering plane (see reference 2).

Calculations based on the above work are to be found in reference 5. The asymmetry factor of equation (4) for the size parameter x=25 and an index of refraction m = 1.5 is plotted in figure 3 against the orientation angle ϕ. The results are strikingly similar for this wide range of size parameters (0.1 to 50). Perhaps more interesting is the plot of the asymmetry factor against size parameter shown in figure 4 where an average over all orientations is made. We see in this case that the factor seems to converge to the value 0.813.

3. APPLICATION TO THE OPTICAL PROPERTIES OF FIBROUS INSULATION

This application is distinguished from that given in section 2 by calculation of scattering intensities from a cloud or tenuous medium of long cylindrical fibers. Thus, we need to define the averaging procedure, and this turns out to be complicated by the equation of constraint for the scattering of light from an infinite cylinder - the equation (2) of section 2.

One might think (and previous calculations were based on this idea) that an average intensity for
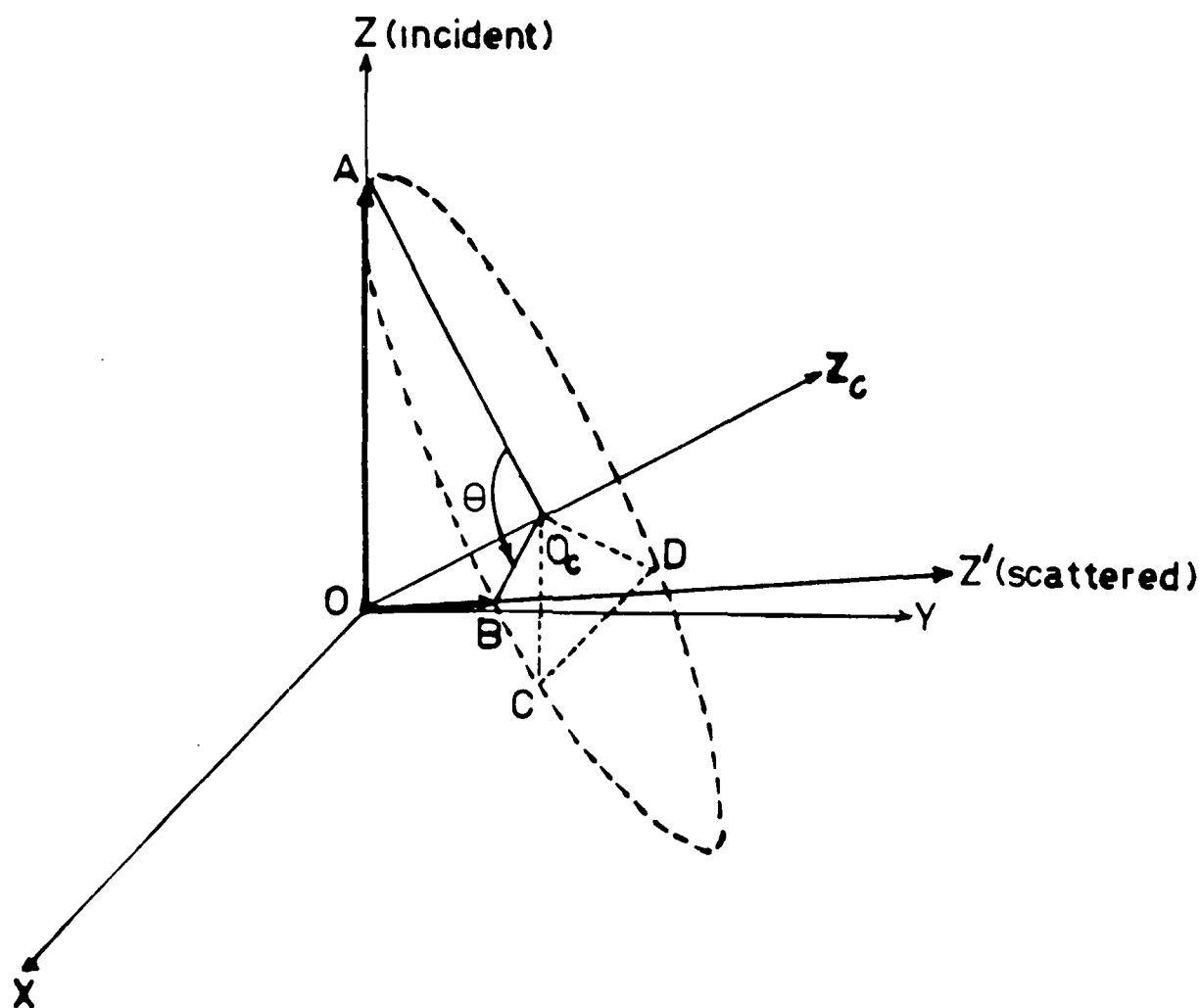
Figure 2. For scattering of light from an infinite cylinder, the scattering is along the element of a cone as shown. The scattering angle θ is measured on the base of the cone counterclockwise from point A (forward direction).

Figure 3. The scattering cone for light scattering from a cylinder with tilt angle $\phi > 45$. The critical scattering angles θ_A and $-\theta_A$ are shown.

11

Figure 4. The asymmetry factor averaged over all possible orientations of the scattering cylinder versus size parameter.

the scattering of light would be given by

$$I_{ave} = (1/4\pi^2) \iint I(\phi,\gamma) \sin \phi \; d\phi \; d\gamma, \tag{5}$$

where I is the scattering intensity, and ϕ,γ are the orientation angles for the cylinder axis as defined in section 2.

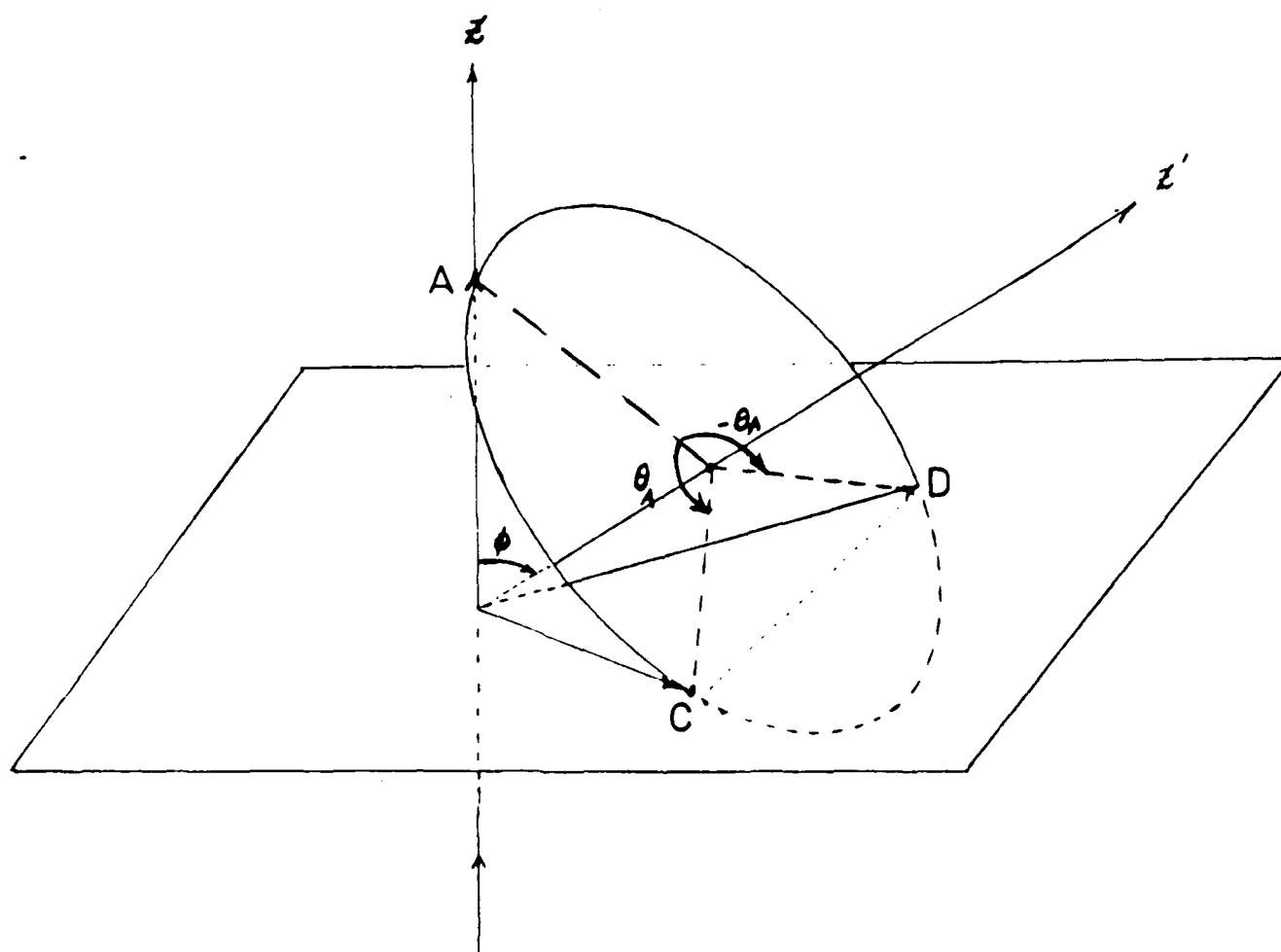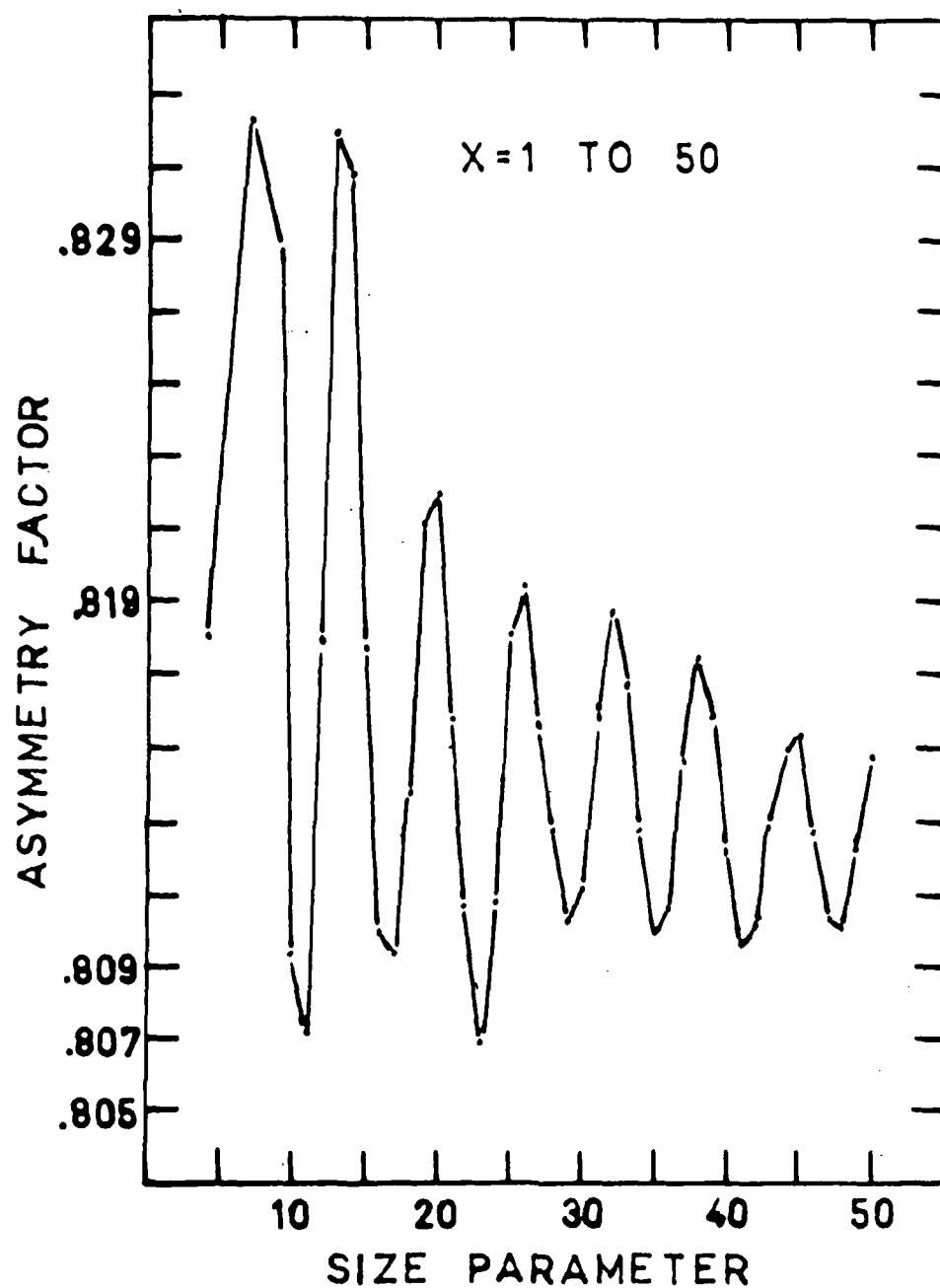The conical scattering pattern from an infinite cylinder complicates the averaging procedure - an equation of constraint is needed. This equation can be derived noting that from first-order scattering theory (Rayleigh-Gans), the scattering intensity from a finite cylinder of height h contains the factor

$$\sin^2(ph/2)/(ph/2)^2$$

where

$$p = k_0 (k_0 - k') k_t .$$

Here, k_0, k', k_t are, respectively, unit vectors in the incident, scattered, and cylinder-axis directions. As the height of the cylinder increases to infinity, this factor vanishes unless $p = 0$, or

$$(k_0 - k') k_t = 0.$$

This is, in effect, the condition that must be satisfied for the scattering from an infinite cylinder to be along the cone (Naturally, the exact theory for the infinite cylinder predict the conic scattering pattern and would give rise to the same condition). Using the geometry given in figure 1, this implies that

$$(k_0 - k') k_t = \{k_0 - [\cos(2\phi_0) k_0 + \sin(2\phi_0) i_0]\}$$

$$x[\sin(\phi) \cos(\gamma) i_0 + \sin(\phi) \sin(\gamma) j_0 + \cos(\phi) k_0]$$

$$= 0,$$

or

$$\phi = \tan^{-1} (\tan(\phi_0)/\cos(\gamma)) \tag{6}$$

We want to emphasize at this point that equation (6) was derived by us [6] and used for the purpose of summing over orientations for the first time in the literature. If we note figure 5, the orientations of the cylinder axis consistent with a scattering angle of $2\phi_0$ and equation (6) follows a great circle path from point A to point B, and for a unit sphere, the length of this path is
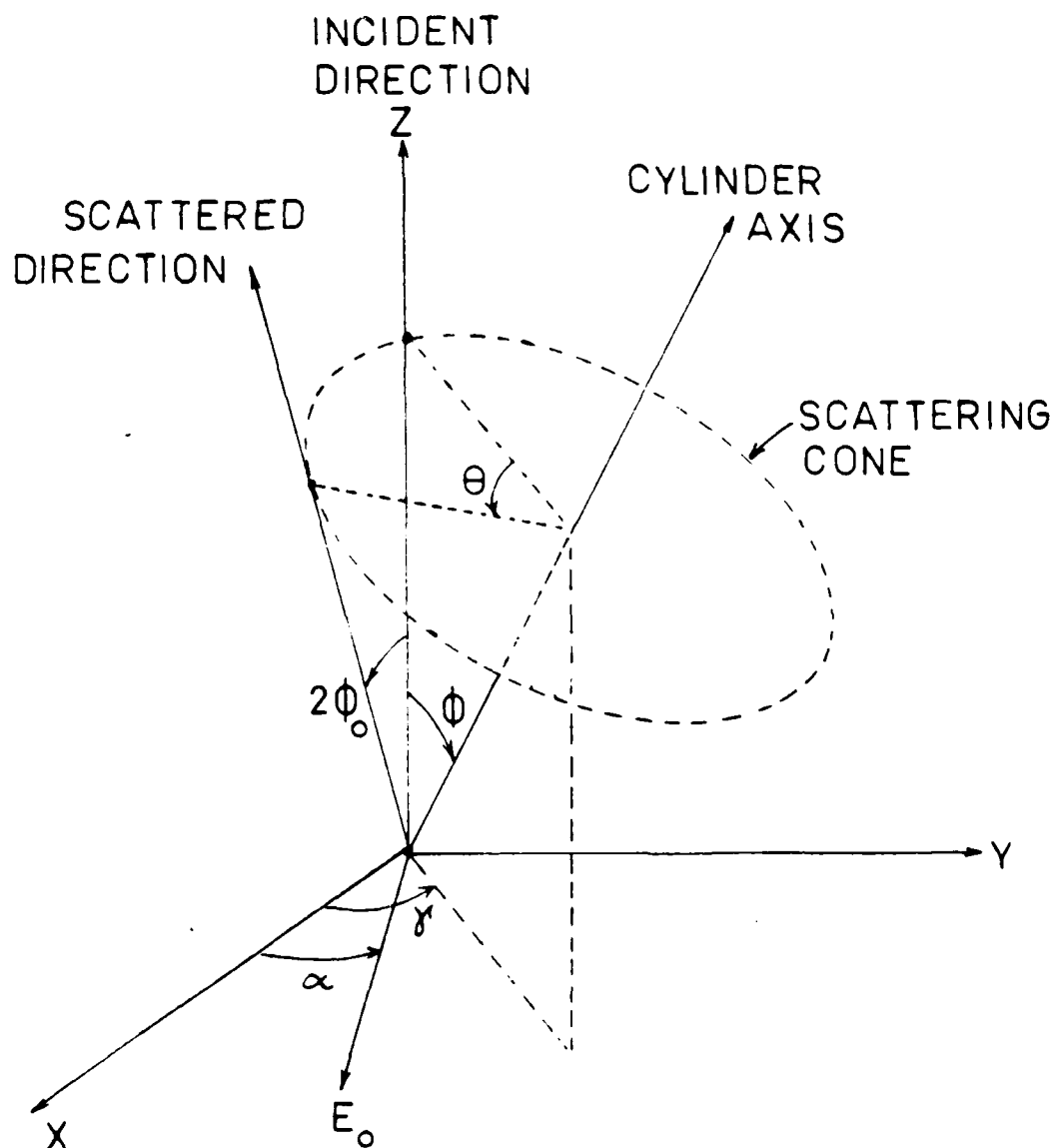
Figure 5. The scattering geometry shown in the reference frame x,y,z, where the x-z plane is the scattering plane. The orientation angles of the cylinder axis are ϕ and γ, and the polarization angle of the linearly polarized wave $\mathbf{E_0}$ is α. The scattering angle between the directions of incidence and scattering is denoted $2\phi_0$. The scattering angle used in the theory for the infinite cylinder is measured in a plane perpendicular to the cylinder axis, and it is denoted θ.

$$\int_A^B ds = \int_0^{\pi/2} d\gamma \, \sin^2(\phi)/\sin(\phi_0) = \int_0^{\pi/2} d\gamma \, /(1 - \cos^2\phi_0 \sin^2\gamma)$$
$$= \pi/2.$$

Therefore, the average intensity for the scattering of light from a cloud of randomly oriented long cylinders is

$$I_{ave} = (1/2\pi) \int_0^{2\pi} I(\phi(\gamma), \gamma) \sin^2(\phi)/\sin(\phi_0) \, d\gamma \qquad (7)$$

The intensities to be averaged are denoted I_1 and I_2, as already noted, and correspond to scattering in and normal to the scattering plane. For an infinite cylinder, these intensities are given by

$$I_1 = const. \, |b_{0I} + 2 \Sigma \, b_{nI} \cos(n\theta)] \cos \gamma^*$$
$$-i \, [2 \Sigma \, b_{nII} \sin(n\theta)] \sin \gamma^* , \qquad (8)$$

$$I_2 = const. \, |a_{0II} + 2 \Sigma \, a_{nII} \cos(n\theta)] \sin \gamma^*$$
$$-i \, [2 \Sigma \, a_{nI} \sin(n\theta)] \cos \gamma^* , \qquad (9)$$

where the "a" and "b" coefficients are derived in detail in reference 7.

These coefficients are dependent on the size parameter of the cylinder, the index of refraction (which may be complex), and the tilt angle ϕ. The angle $\gamma^* = \gamma - \alpha$, where α is the angle that the incident electric field makes with the scattering plane.

We have made three applications. The first is a comparison with the work of McKay et. al[8] in which the averaging is done using equation (5) instead of equation (7). We calculate the intensities for light of wavelength 10 microns incident on cylinders with the complex index of refraction m = 1.85 -i 0.033 and size parameter x = 7.3513. These are the values used in reference 8. The results for I_1 and I_2 are shown in figure 6 for the incident light polarized in and perpendicular to the scattering plane ($\alpha=0$ and $\alpha=\pi/2$, respectively). Also shown in figure 6 is the intensity I_{12} where the incident light is polarized in the scattering plane and the scattered light is polarized perpendicular to the scattering plane.

The salient results are:

(1) A strong forward scattering value. This is in contrast to the results of reference 8 where the intensities go to zero in the forward direction as a result of compensating for a singularity that occurs because of an incorrect averaging procedure.

(2) Smaller values in the region of 70 to 150 degrees of scattering.

(3) A backscatter value approximately 1 to 2 orders of magnitude smaller than the forward scattering value.

(4) The number of maxima roughly equal to the value of the size parameter.
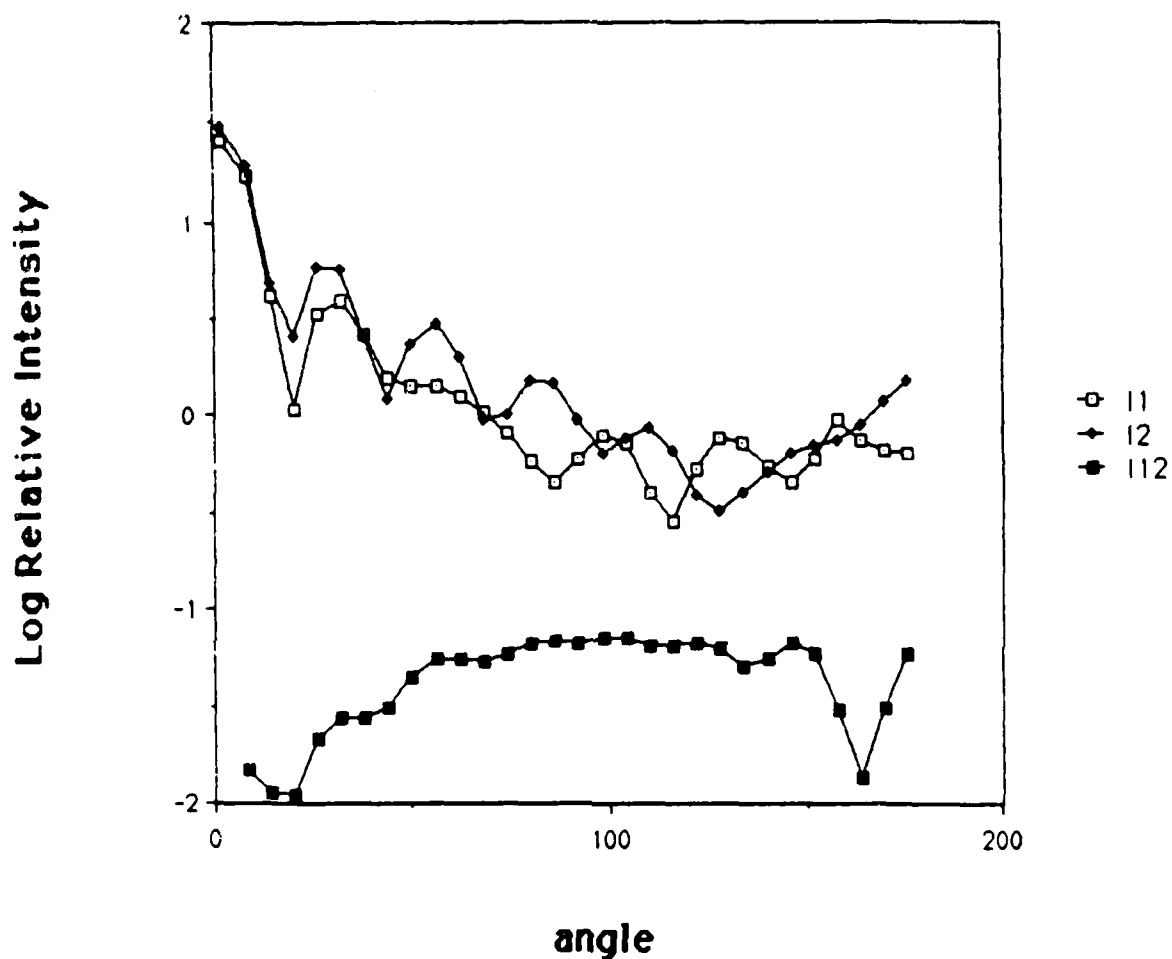
Figure 6. The relative intensities defined in equation 9 versus the scattering angle $2\phi_0$. The top curves are I_1 for $\alpha = 0$ and I_2 for $\alpha = \pi/2$. The bottom curve is I_2 for $\alpha = 0$ (or I_1 for $\alpha = \pi/2$). The size parameter $x = 7.3513$ and $m = 1.85 - 0.033i$.

16

Figure 7. The relative intensities defined in equation 9 versus the scattering angle $2\phi_0$ for x = 17.173 and m = 1.29 - 0.0954 i. a) The results of reference 3. b) our corrected results.

17

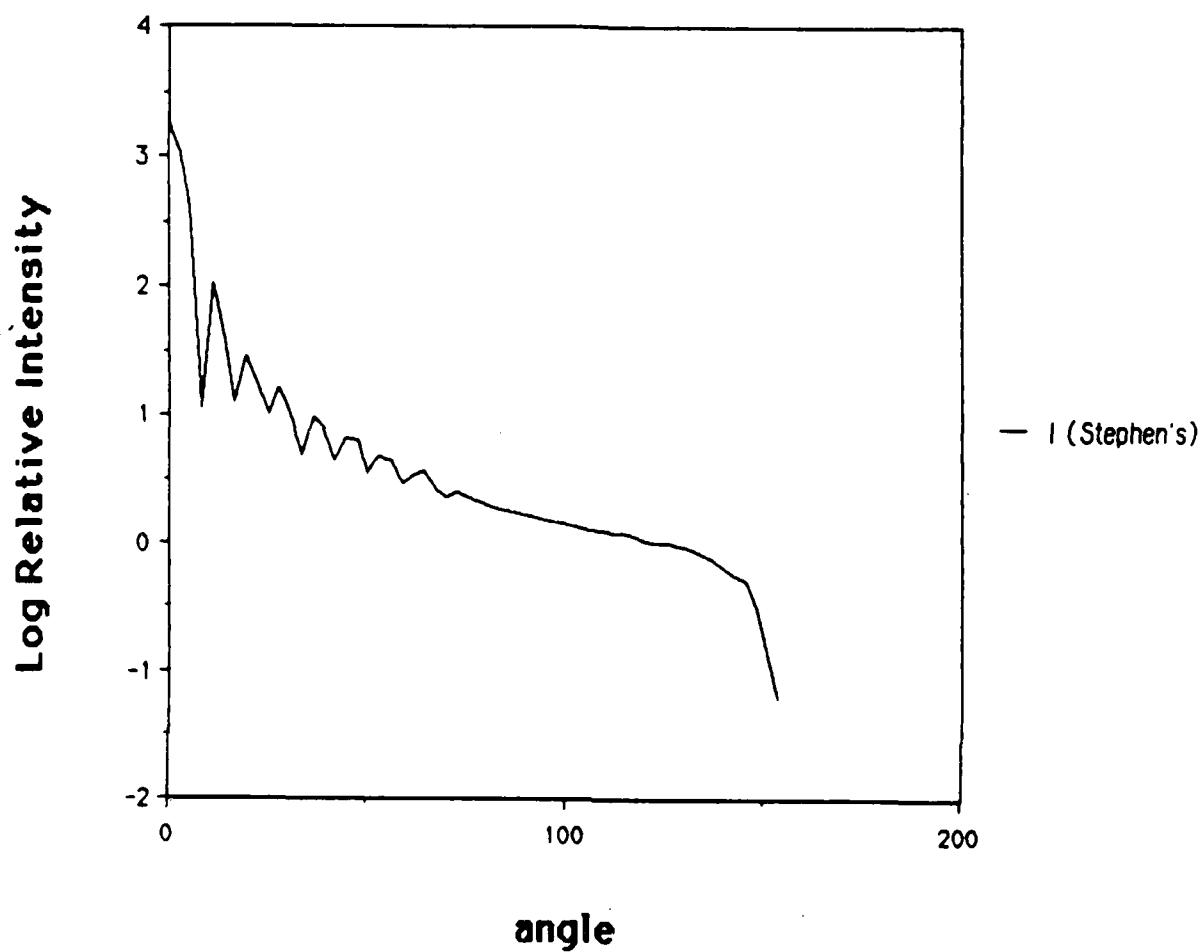Figure 8. The relative intensities defined in equation 9 versus the scattering angle $2\phi_0$ for $x = 17.173$ and $m = 1.29 - 0.0954$ i. a) The results of reference 3. b) our corrected results.
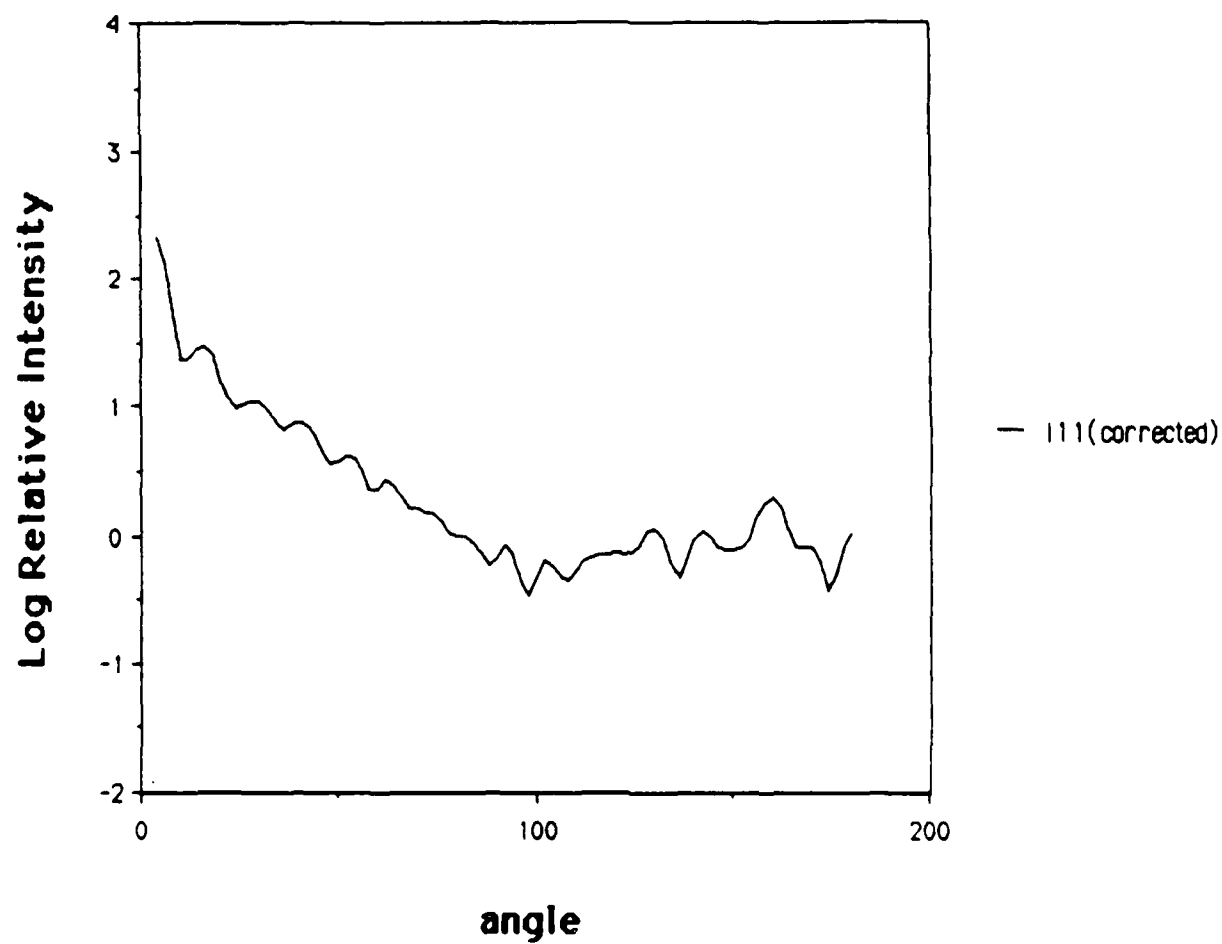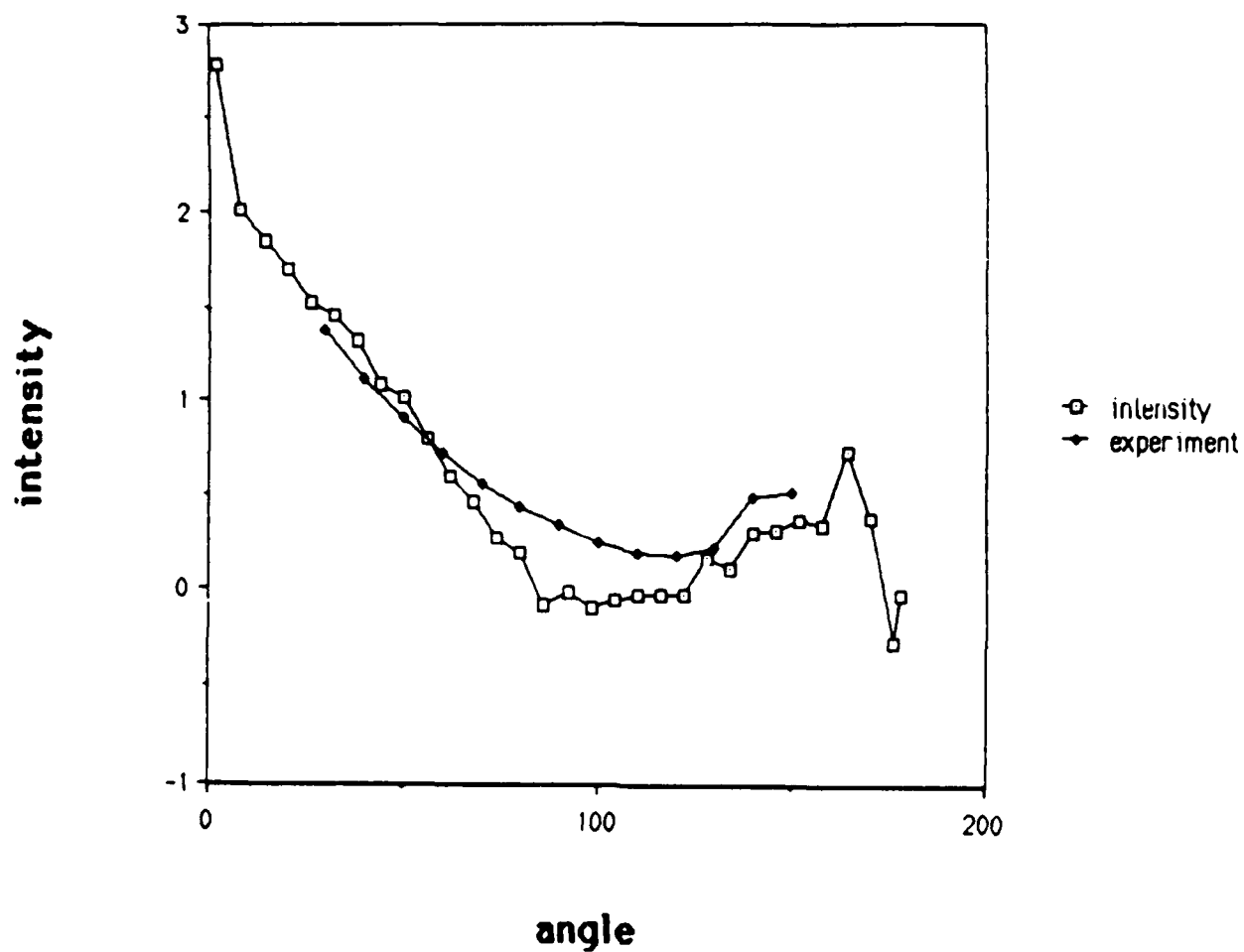
Figure 9. The relative intensity defined in equation 9 versus the scattering angle for x = 45.7 and m = 1.31. The experimental results are shown by black diamonds and our theoretical results are shown by open squares.

The second application is a comparison with the work of Stephens[9] which also used the wrong averaging procedure to determine the effect of the scattering of thermal radiation from randomly oriented ice crystals (which are long hexagonal prisms).

We calculate intensities for light of wavelength 11 microns , index m = 1.29 -i 0.0954, and size parameter x = 17.136. The results are shown in figures 7 and 8 (ours and Stephens, respectively). Our results show marked differences especially at the larger scattering angles, where our results continue to show fluctuations over the full angular range.

Finally, we make a comparison of our averaging procedure with the experimental results of Huffman et al.[10] In this experiment, visible light of wavelength 0.55 microns is incident on ice crystals whose size parameter is x = 45.7 and m = 1.31. The results are shown in figure 9 where the experimental points are shown as black diamonds and the theory as open squares. We see general agreement over the whole range of the experiment (for 10 to 150 degrees) . In particular, we note that agreement is achieved at the largest scattering angle of 150 degrees.

4. THE SCATTERING OF LINEARLY POLARIZED LIGHT FROM RANDOMLY ORIENTED SHORT CYLINDERS AND SPHEROIDS

In contrast to the first two sections, we now study the scattering of light from finite cylinders and spheroids of the same material, equal volume, and the same aspect ratio (length/diameter). These aspect ratios range from 10 down to 0.1. The purpose of this study is to determine if randomizing the target orientation effectively negates the differences in shape for these targets. The iterative approach of Shifrin and Acquista[11,12] is used.

The theory for the scattering of light from a finite cylinder arbitrarily oriented relative to the incident light is given in reference 1 and this includes the derivation of the second-order iteration that effectively includes the self-interaction of the various parts of the target. An application to finite cylinders and spheroids of equal volume and aspect ratio was done in reference 13. In reference 13, the second-order effect is evaluated and found to be less than 15% for the following target parameters:

$$m = \text{index of refraction} = 1.5,$$

$$\text{target volume} <= 1 \ (\mu m)^3,$$

$$\lambda = \text{wavelength of light} = 2\pi \ (\mu m).$$

4 A. THEORY

A brief outline of the theory may be useful. The outgoing-wave solution to the Maxwell's equation is

$$E(r) = E_o \exp(ik_o r) + \nabla \times \nabla \times \int d^3 r' \ [(m^2 - 1)/(4\pi)] \ U(r') \ E(r')$$

$$\times \exp(ik_o |r - r'|)/|r - r'| \ -(m^2 - 1) \ E(r) \tag{10}$$

where U(r) is one inside the target and zero outside the target to allow the integration to extend over all space. The electric field is next expressed as

$$E_i(r) = A_{ij} E_{eff,j}(r) \tag{11}$$

where A is the polarization matrix for the target. This matrix represents the effect of the polarization charge induced within the target by the field, and it would be expected to be a function of the internal space of the target and the field variables. In the limit of long wavelengths, however, this matrix takes a very simple form - a constant diagonal matrix for spheres and infinite cylinders. Since we do not know what A is, we assume a simple form as the basis for an iterative approach. This form is

$$A = \text{ unit matrix , outside the target}$$

$$A = \begin{vmatrix} a_{TE} & 0 & 0 \\ 0 & a_{TE} & 0 \\ 0 & 0 & a_{TM} \end{vmatrix} \text{ , inside the target} \tag{12}$$

Here, i = 3 corresponds to the target axis (TE means transverse electric and TM means transverse magnetic). The effective field is next expanded in powers of

$$\beta = (m^2 - 1) / (4\pi) \tag{13}$$

as

$$E_{eff}(r) = E_0 \exp(ik_0 r) + \Sigma_n \beta^n E^{(n)}_{eff}(r) \; , \tag{14}$$

and this is substituted into equation (10) using equations (11) and (12). Each term in the series can then be determined from the previous term starting with

$$E^{(0)}_{eff}(r) = E_0 \exp(ik_0 r) .$$

This is the Shifrin approach that we have generalized for a plane wave incident on a target from an arbitrary direction and with arbitrary polarization.The details of the method along with the first two orders of iteration are given in references 12 and 13. For example, the first-order term is

$$E^{(1)}_{eff}(r) = (k_0^2 \exp(ik_0 r)/r)\, u(k_0\, \mathbf{r} - \mathbf{k_0})\, x[a_{TE}(E_{oxt}\, \mathbf{i_t} + E_{oyt}\, \mathbf{j_t}) + a_{TM}\, E_{ozt})],\qquad(15)$$

where $\mathbf{x} = \mathbf{r}\, x\, \mathbf{r} - \mathbf{x}$, and the function u is the Fourier transform of the pupil function for the target:

$$u(\mathbf{x}) = \int d^3 r'\, U(\mathbf{r})\, \exp(i\, \mathbf{x} \cdot \mathbf{r}').\qquad(16)$$

The forms of u for finite cylinders and spheroids are given in reference 13.

4 B. THE AVERAGING PROCEDURE FOR FINITE CYLINDERS AND SPHEROIDS

We now turn to the averaging procedure for cylinders and spheroids, which is actually easier than for very long cylinders as discussed in section 3. Refering to figure 10 , we recall the reference frame (x_0, y_0, z_0) , where the incident direction is z_0 and x_0 is in the scattering plane. The target frame has z_t along the target axis and x_t in the plane containing z_t and z_0 (x_t, y_t, z_t) .The incident field makes an angle α with the reference plane , and so the components of $\mathbf{E_0}$ in the target frame , required for equation (15) are given by

$$
\begin{vmatrix} E_{oxt} \\ E_{oyt} \\ E_{ozt} \end{vmatrix} = R_{yt}(\phi)\, R_{zo}(\gamma) \begin{vmatrix} E_0 \cos\alpha \\ E_0 \sin\alpha \\ 0 \end{vmatrix}
$$

$$
= E_0 \begin{vmatrix} \cos\phi\cos\gamma\cos\alpha + \cos\phi\sin\gamma\sin\alpha \\ -\sin\gamma\cos\alpha + \cos\gamma\sin\alpha \\ \sin\phi\cos\gamma\cos\alpha + \sin\phi\sin\gamma\sin\alpha \end{vmatrix}\qquad(17)
$$

The scattered wave is next obtained using the Shifrin series in the target frame of reference, and it must be transformed by the inverse of the transformation used in equation (17) back to the reference frame.These components are denoted $(E_{sxo}, E_{syo}, E_{szo})$ Finally, a frame x', y', z' is define with z' in the scattered direction and x', z' in the same plane as x_0, z_0 , and the components of the scattered field are related to this frame:

$$
\begin{vmatrix} E_{sx'} \\ E_{sy'} \\ E_{sz'} \end{vmatrix} = R_{yo}(2\phi_0) \begin{vmatrix} E_{sxo} \\ E_{syo} \\ E_{szo} \end{vmatrix}\qquad(18)
$$

We can now define two intensities:

Figure 10. The geometry for the scattering process. The directionof incidence is z_0, the direction of scattering is z', the symmetry axis of the target is z_A, and the incident electric field intensity is E_0. The reference plane is x_0-z_0, and this plane contains z'. E_0 is in the x_0- y_0 plane and makes an angle α with the reference plane. The reference plane is (x_0, y_0, z_0), and the target frame is (x_A, y_A, z_A).

$$I = (k_o{}^2 r^2 / E_o{}^2) \; [|E_{sx'}|^2 + |E_{sz'}|^{2P}],$$

$$I = (k_o{}^2 r^2 / E_o{}^2) \; |E_{sy'}|^2. \tag{19}$$

These represent the intensities for the scattering of an incident beam of light from a target with an arbitrary orientation. For light incident on a cloud of randomly oriented targets, all possible orientations must be included. Thus, an average over the orientation variables must be taken

$$I_{ave} = (1/2\pi) \int d\gamma \int d\phi \; \sin\phi \; I(\gamma, \phi) \tag{20}$$

4 C. APPLICATIONS

Figures 11 through 14 show the averaged intensities I_1 and I_2 versus ϕ for the scattering of linearly polarized light from short cylinders and spheroids. The incident polarization is in the reference plane, and the respective aspect ratios are 10, 2, 1, and 0.1. The targets have a volume 1 $(\mu m)^3$. This volume is chosen so that the first order in the iterative method accounts for at least 85% of the scattering effect as shown in reference 13.

The amplitudes for the sphere are shown as dashed lines, while the amplitudes for the finite cylinder are shown as solid lines with dots. The results for spheroids are shown as solid lines with crosses. The results for a sphere are shown on each graph as a reference.

For the average intensity I, the results for a spheroid and a finite cylinder of the same volume and aspect ratio are quite similar except for the minimum point. The long spheroid behaves like a cylinder while the short spheroid behaves like a sphere. On the other hand, intensities I for the finite cylinder and spheroid differ markedly for the shorter aspect ratios (the values for the spheroid are zero for the aspect ratio of one, and they are too small to appear on the graph for the aspect ratio 0.1.Therefore, spheroids and finite cylinders of the same material and volume create similar scattering patterns if the plane of linear polarization is not changed by the scattering, if the orientations are random , and if an average is taken. If the plane of polarization is changed by the scattering, even the averaging process does not obliterate differences between the two shapes. Reference 6 details the calculations and results.

5. SCATTERING FROM TARGETS FORMED FROM AN ASSEMBLY OF CIRCULAR DISKS

In this section we will describe a new model for computing the scattering characteristics of dielectric objects whose shapes may be quite complex. The model assumptions are: 1) the target has a central axis that may be curved, and the cross section at each point on this axis is circular, and 2) the wavelength is larger than the target dimension that can produce standing waves. This second assumption can be relaxed if a better polarization matrix is used to initiate the calculation as will be discussed later.This calculational model is then applied to two cases whose scattering characteristics are
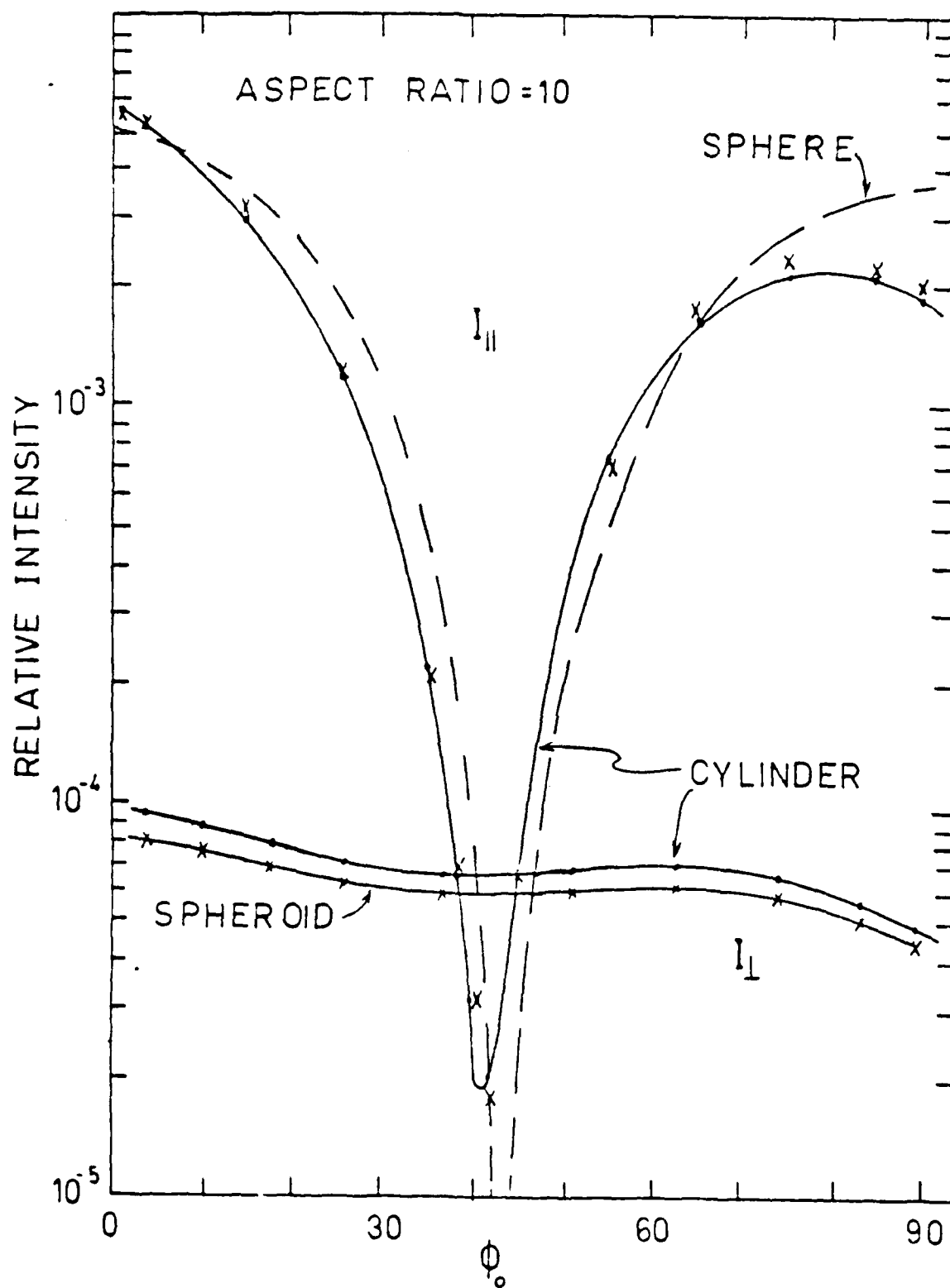
Figure 11. The intensities I and I for targets of various shapes, all with volume 1 $(\mu m)^3$. The index of refraction of each is m = 1.5. The results for a spherical target are shown as dashed lines (I = 0). The results for a cylinder and a spheroid of aspect ratio (length/diameter) 10 are shown as solid lines (dots for the cylinder and crosses for the spheroid).
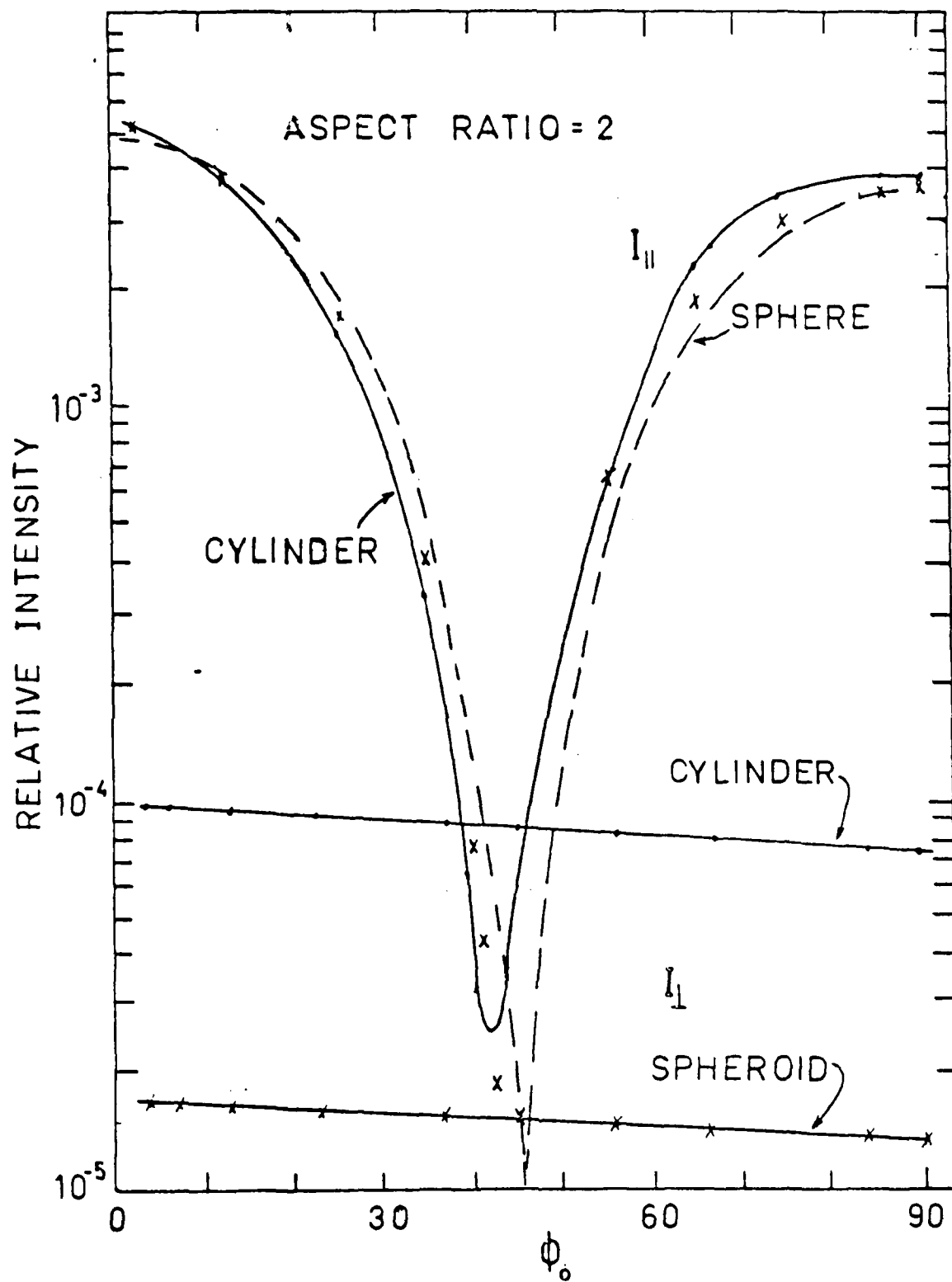
25

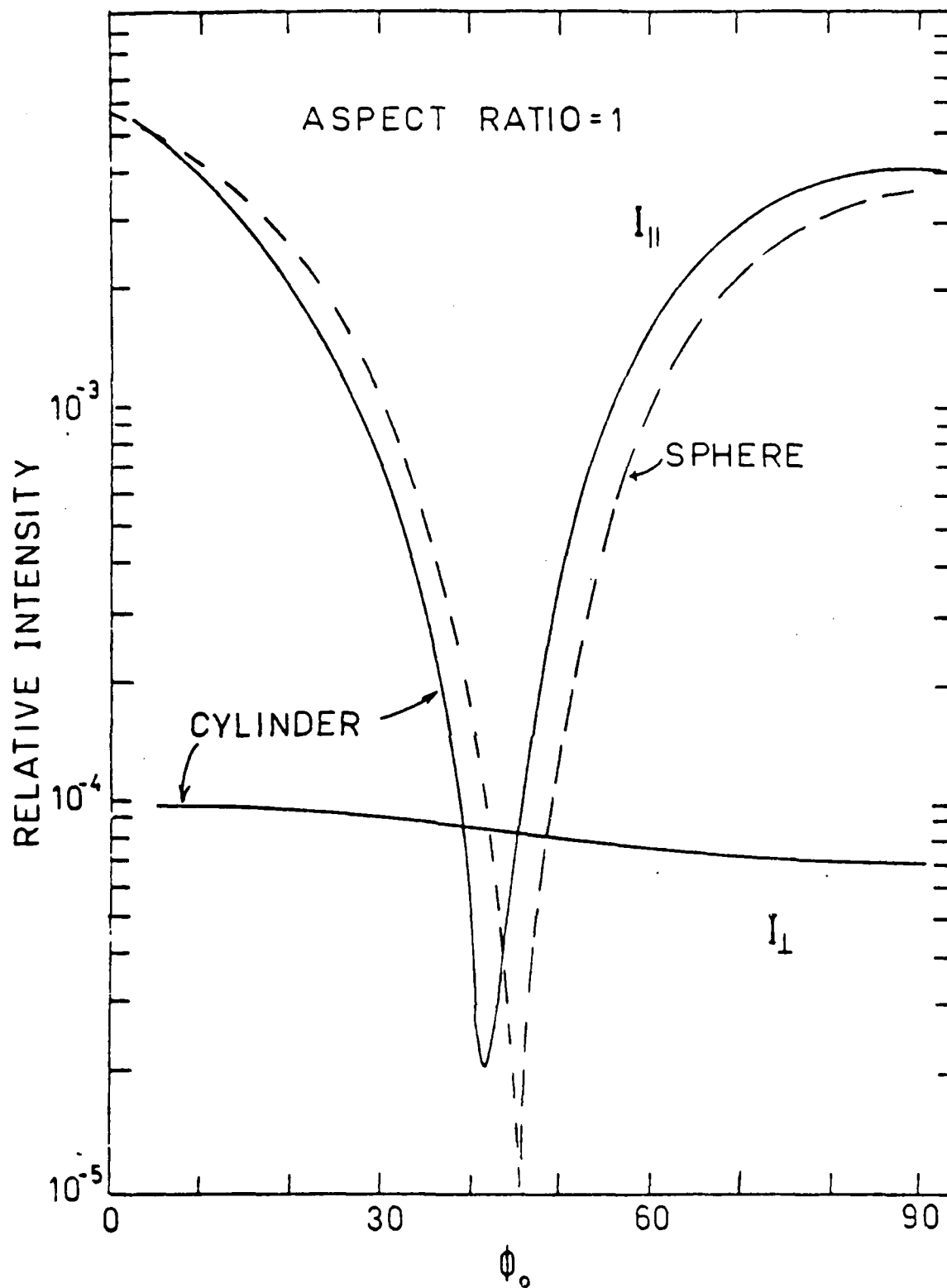Figure 12. The same as in figure 11 for an aspect ratio of 2.

26

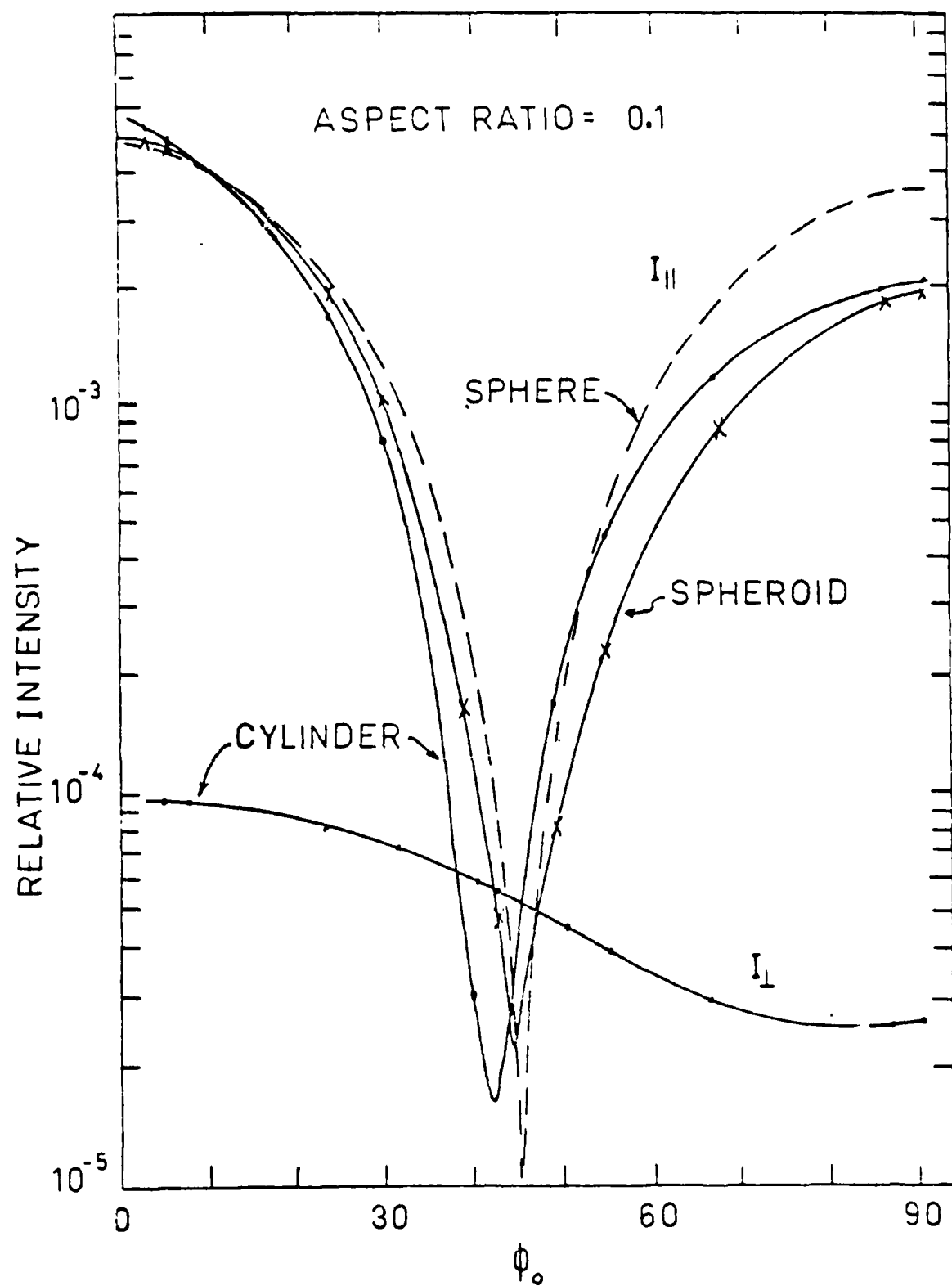Figure 13. The same as in figure 11 for an aspect ratio of 1, where the sphere and spheroid are identical.

Figure 14. The same as in figure 11 for an aspect ratio of 0.1. Note that the intensity I for the spheroid is less than 10^{-5} for the spheroid and hence does not appear on this graph.

28

well known from other computational schemes, first a finite dielectric cylinder and secondly a dielectric spheroid (whose scattering characteristics can be computed exactly). The technique is then applied to the case of a dielectric helix. In this application the "Circular Intensity Differential Scattering (CIDS)" is computed and the results are compared with the calculations of Bustamente et. al. who computed CIDS for a helix made of a string of dipoles. The similarities between the two calculations is striking. A second series of computations involve the scattering of linearly polarized light by a helix. The particle parameters were chosen to match the experimental particle used by Dr. R.T.Wang who measured the scattering of microwaves by a dielectric helix. Once again the comparison between the calculation and the experimental results are quite good, thereby lending further credibility to the calculational scheme. The final application of this section will be a comparison of the scattering of light from a toroid and oblate spheroid of the same volume and similar radius and height. We study the signatures of these shapes for different wavelengths of incident light.

We consider the scattering of light from non-magnetic dielectric targets with an index of refraction m. Maxwell's equations lead to an integral equation for the final-state electric field satisfying the outgoing spherical wave boundary condition [1,6,11,12,13]:

$$E_i(r) = E_{inc,i}(r) + \alpha \int dV' D_{ij} G(r,r') E_j(r'), \tag{21}$$

where the integration is over the volume of the dielectric target. The elements of this integral equation are

$$E_{inc}(r) = E_0 \exp(ik_0 \ r) = \text{incident plane wave},$$

$$D_{ij} = \partial/\partial x_i \ \partial/\partial x_j + k_o^2 \ \delta_{ij} , \tag{22}$$

$$G(r,r') = \exp(i \ k_0 \ |r - r'|)/|r - r'| ,$$

$$\alpha = (m^2 - 1)/(4\pi),$$

where the incident plane wave is assumed to be harmonic with the time factor $\exp(i\omega t)$, and where $k_0 = 2\pi/\lambda$.

In our previous papers, we used the Shifrin technique which takes as the basis for an iterative solution the replacement

$$E_k(r') \ \text{-----} \text{>} \ (A_{jk})\text{electrostatic} \ E_{inc,k}(r') \ . \tag{23}$$

with the assumption that the matrix A is constant over the entire volume of the target. This allows the analytic evaluation of the first-order effect through the use of Fourier transforms. The technique is shown to work well for dielectric spheres, finite cylinders, and spheroids provided the diameter of the

target is smaller than the wavelength of the incident light. For example, for a long dielectric cylinder, we have

$$(A)_{electrostatic} = \begin{vmatrix} a_{TE} & 0 & 0 \\ 0 & a_{TE} & 0 \\ 0 & 0 & a_{TM} \end{vmatrix} \quad (24)$$

with $a_{TE} = 2/(m^2 + 1)$ and $a_{TM} = 1$.

However, for more complex target shapes, the replacement (23) cannot be expected to hold as A should be expected to vary over the target. We are therefore proposing a model that allows for such a variation while retaining in part the Fourier transform technique. If the target has a circular cross section at every point along its central axis, we can divide the target into disks which are perpendicular to the axis and of infinitesimal thickness. We then assume that the polarization matrix is constant within each disk. However, the matrix is permitted to vary from disk to disk. Thus, the integration in equation (21) is divided into disks and

$$E_i(r) = E_{inc,i}(r) + \alpha \sum \int dV' \, D_{ij} \, G(r,r') \, A_{jk}^l \, E_k(r') \quad (25)$$

where the sum is over the disks that compose the target, and the integral is over the lth disk in which A^l is constant.

An expansion is then based on the replacement

$$A_{jk}^l \, E_k(r') \text{------} A_{jk}^l \, E_{inc,k}(r') \quad (26)$$

where A^l is a constant matrix tailored to the application as the second model assumption. The expansion is in powers of α :

$$E(r) = E_{inc}(r) + \sum \alpha^n \, E^{(n)}(r). \quad (27)$$

5 A.   THE FIRST ORDER CONTRIBUTION.

Putting the expansion (27) into equation (25) gives the first-order term:

$$E_i^{(1)}(r) = \sum \int dV' \, [D_{ij} \, G(r,r')] \, A_{jk}^l \, E_{inc,k}(r')$$

$$= \sum I^l(r) , \quad (28)$$

where the summation is over the disks. The disk integral I^l can be evaluated by means of Fourier transforms if it is first converted to an integral over all space as

$$I_i^l(r) = \int dV' \, [D_{ij} \, G(r,r')] \, A_{jk}^l \, E_{0,k} \, \exp(i \, k_o \, r') \, U(r'),$$ (29)

where the pupil function $U(r')$ is unity if r' is within the target and zero if r' is outside the target. Defining the Fourier transforms by

$$G(r,r') = 1/(2\pi)^3 \int d^3p \; g(p) \, \exp(i \, p \, (r - r') \,),$$

$$D_{ij} \, G(r,r') = 1/(2\pi)^3 \int d^3p \; g(p) \, [k_o^2 \, \delta_{ij} - p_i \, p_j] \, \exp(i \, p \, (r - r') \,), \quad \text{and}$$

$$U(r') = 1/(2\pi)^3 \int d^3q \; u(q) \, \exp(i \, q \, r'),$$ (30)

we evaluate

$$g(p) = g(p) = 4\pi/(p^2 - k_o^2),$$ (31)

and

$$u^l(q) = 2\pi \, a_l^2 \, dz_l \, J_1(q \, a_l)/(q \, a_l) \; \exp(i \, q \, h_l).$$ (32)

Equation (10) is the Fourier transform of the pupil function for a disk of radius a_l and thickness dz_l. The vector q has the component q perpendicular to the axis of the disk, and h is the vector from the center of the observers coordinate system to the center of the lth disk.

The assumpion that the matrix A^l is constant over the disk allows us to integrate over the r' space leaving, after application of the convolution theorem

$$I_i^l(r) = 1/(2\pi)^3 \int d^3p \; u^l(p - k_0) g(p) (k_o^2 \, A_{ik}^l - p_i \, p_j \, A_{jk}^l) \, E_{0,k} \, \exp(i \, p \, r).$$ (33)

We now make the far-field approximation to complete the integration, choosing the z direction of p-space to be along the unit vector r - directed from the center of the target to the field point:

$$I_i^l = 1/(2\pi)^3 \int p^2 dp \int d\phi \int d\cos(\phi) \, \exp(ipr\cos(\phi)) \, u^l(p - k_0) \, g(p)$$

$$(k_o^2 \, A_{ik} - p_i \, p_j \, A_{jk}^l) \, E_{0,k} \, .$$

Integration by parts, ignoring terms of order $1/r^2$ and higher gives

$$I_i^l = k_o^2 \, \{\exp(i \, k_o \, r)/r\} \, u^l(k_o \, r - k_0) \, [A_{ik}^l - r_i \, r_j \, A_{jk}^l] \, E_{0,k} \, ,$$ (34)

where r_1, r_2, and r_3 are orthogonal unit vectors with r_3 aligned along the axis of the lth disk. Substitution of equation (34) into the expression for the first-order field, equation (28), gives

$$E_i^{(1)}(r) = 2\pi \{ \int ds \, a^2(s) \, J_1(q \, (s) \, a(s))/(q \, (s) \, a(s)) \, \exp(i \, q(s) \, h(s) \,)$$
$$k_o^2 \, (A_{ik}(s) \, - \, r_i \, r_j \, A_{jk}(s) \,) \, E_{o,k} \,) \} \, \exp(i \, k_o \, r)/r. \tag{35}$$

The vector q is the transfer of momentum during scattering, $k_o(r - k_o)$, with the unit vector k_o pointing along the direction of incidence. In equation (35) the sum over 1 has been replaced by an integration along the main axis of the target, denoted by s. We will see in the applications, that the frame of reference to be used is suited to the lth disk with the disk-z axis along the axis of the disk. In this frame, A will be assumed constant and diagonal.

5 B. THE SECOND ORDER CONTRIBUTION.

Returning to the expansion of the final-state electric field, equation (25),the second-order term is

$$E_i^{(2)}(r) = \sum \int dV' \, [D_{ij}G(r,r')] \, A_{jk}^l \, E_k^{(1)} \, (r') \, U_l(r'), \tag{36}$$

where $E^{(1)}$ is the first-order term within the target:

$$E_k^{(1)}(r) = \sum \, I_k^l(r)$$

$$= 1/(2\pi)^3 \, \sum \, \int d^3p \, u^l(p - k_o) \, g(p)$$

$$(k_o^2 \, A_{km}^{l'} \, - \, p_k \, p_n \, A_{nm}^{l'}) \, E_{o,m} \, \exp(ipr') \tag{37}$$

Introduction of the Fourier transforms in eqs. (30) allows the integration of r'-space leaving

$$E_i^{(2)} \, (r) = 1/(2\pi)^3 \, \sum \, \sum \, \int d^3p' \int d^3p \, g(p') \, [k_o^2 \, \delta_{ij} \, - \, p'_i \, p'_j \,]$$

$$x u^l(p' - p) \, u^{l'}(p - k_o) \, g(p)$$

$$x A_{jk}^l \, [k_o^2 \, A_{km}^{l'} \, - \, p_k \, p_n \, A_{nm}^{l'} \,] \, E_{o,m} \, \exp \, p \, r \tag{38}$$

We next make the far-field approximation which allows the integration over p-space using integration by parts ignoring terms of the order of $1/r^2$, the result is

$$E_i^{(2)} \, (r) = \exp(i \, k_o \, r)/(4\pi r) \, \sum \, \sum \, \int d^3p \, g(p) \, [k_o^2 \, \delta_{ij} \, - \, p_i \, p_j \,]$$

$$x u^l(p - k_o \, r \,) \, u^{l'}(k_o \, r - k_o) \, A_{jk}^l$$
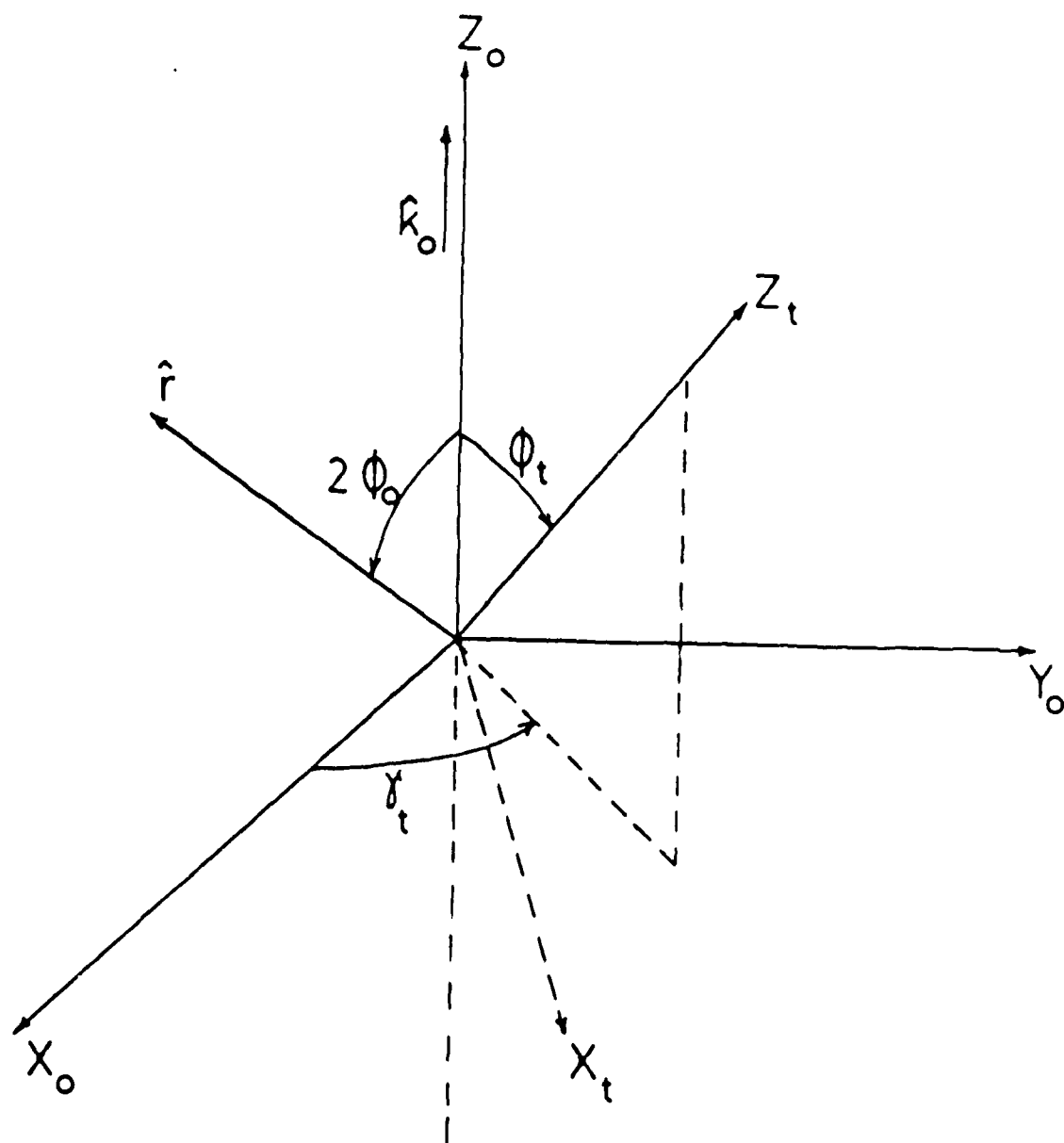$$x \, [A_{km}^{l'} \, - \, r_k \, r_n \, A_{nm}^{l'} \,] \, E_{o,m} \tag{39}$$

Figure 15. The reference frame (0) and the target frame (t). Light is incident along the z_0 axis and scattered along **r**. The symmetry axis of the target is along z_t, and this axis is oriented by the polar angle δ_t and the azimuthal angle γ_τ.

33

The summations will become integrations over the symmetry axis of the target, and so there is a five-fold integration to be performed

6. APPLICATIONS TO TARGETS WITH A LINEAR SYMMETRY AXIS
6 A. THE FINITE DIELECTRIC CYLINDER

The results of this application without the decomposition into small disks have already been presented in Refs. 6 and 13 . Although there is no need to divide this target into infinitesimal disks when the polarization matrix is assumed to be constant within the cylinder (Shifrin approximation), it is nevertheless instructive to use the cylinder to show how the disk technique works. On the other hand, this decomposition would be necessary if we wanted to apply the results of reference 13 which demonstrated that A does indeed vary over the cylinder volume for short cylinders.

The cylinder geometry is shown in Fig. 15. The reference frame (x_0, y_0, z_0) is defined with z_0 along the direction of the incident light, and the X_0 axis is chosen such that the scattered direction r, lies in the X_0-Z_0 plane. The target frame (x_t, y_t, z_t) is defined with z_t along the symmetry axis of the cylinder, and the X_t axis is chosen so that the direction of incidence, z_0 lies in the x_t-z_t plane. If the polar and azimuthal angles of z_t are denoted ϕ_t and γ_t , respectively, the reference and target frames are related as

$$X_{t,i} = T_{0 \to t, ij}\ X_{0,j} \tag{40}$$

with the transformation matrix given by

$$T_{0 \to t} = \begin{vmatrix} \cos \phi_t \cos \gamma_t & \cos \phi_t \sin \gamma_t & -\sin \phi_t \\ -\sin \gamma_t & \cos \gamma_t & 0 \\ \sin \phi_t \cos \gamma_t & \sin \phi_t \sin \gamma_t & \cos \phi_t \end{vmatrix} \tag{41}$$

In the target frame of reference the polarization matrix is both constant and diagonal:

$$A = \begin{vmatrix} a_{TE} & 0 & 0 \\ 0 & a_{TE} & 0 \\ 0 & 0 & a_{TM} \end{vmatrix} \tag{42}$$

For a long cylinder (aspect ratio = length/diameter > 20), the matrix elements in the long wavelength limit are given in equation (4). For shorter cylinders, reference 13 gives values obtained in the long-wavelength limit where the values for disks nearer the edges differ significantly from those nearer the center.

The first-order contribution to the final-state electric field has its components first expressed in the target frame to take advantage of the form in equation (22):

$$E^{(1)}(r) = 2\pi a^2 k_o^2 J_1(q\,a)/(q\,a)\ \exp(i\,k_o r)/r$$

$$\times\ [a_{TE}(E_{oxt}\,i_t + E_{oyt}\,j_t) + a_{TM}\ E_{ozt}\,k_t\ ]_{transverse}$$

$$\times \int dz\ \exp(i\,q\,z) \tag{43}$$

Here, "transverse" denotes that portion of the vector transverse to the scattered direction of light:

$$X_{transverse} = X - X\,r\ r\ .$$

Moreover,

$$q\ =\ |k_o\,(r - k_o) \times k_t\ |,$$
$$q\ =\ k_o\,(r - k_o)\ k_t\ , \tag{44}$$

where k_t is a unit vector along the symmetry axis of the cylinder, a is the radius of the cylinder, and h is the height of the cylinder.

The incident wave is assumed to be linearly polarized in this application:

$$E_o\ =\ E_{oxo}\,i_o + E_{ozo}\,j_o \tag{45}$$

in the reference frame, and E_o makes an angle α with the x_o axis. The components of E_o used in eqation 43 are in the target frame, thus the transformation (20) is used. Evaluation of the integral in equation 43 gives the result derived in reference 13:

$$E_i^{(1)}(r)\ =\ 2\pi a^2 h\ J_1(q\,a)/(q\,a)\ \exp(i\,k_o\,r)/r\ k_o^2$$

$$[a_{TE}(E_{oxt}\,i_t + E_{oyo}\,j_t) + a_{TM}\,E_{ozt}\,k_t]$$

$$\sin(q\,h/2)/(q\,h/2). \tag{46}$$

As the height of the cylinder increases, the last term will give a significant contribution only when $q = 0$. We show in reference 6 that this gives rise to the scattering being restricted to a volume near the surface of a cone whose symmetry axis lies along the cylinder axis and whose apex half-angle is θ_o. The scattering angle, between k_o and r, is denoted by $2\theta_o$.

This derivation shows that the division of the target into disks and the subsequent coherent addition of

these effects leads to the same first-order result as that derived for the scattering of light from a cylindrical target. We should also emphasize that this new approach is necessary if the polarization matrix varies along the cylinder axis with cylindrical symmetry as was shown to be the case in the same reference. A calculation is now performed for a cylinder of volume 4.8 $(\mu m)^3$ and aspect ratio 5 for incident light of wavelength $1 = 2\pi$ microns. The incident light is linearly polarized in the $x_0\text{-}z_0$ plane. These conditions insure that the first-order calculation is dominant and accurate as shown in reference 13. The polarization matrix elements vary over the cylinder along the symmetry axis x as

$$a_{TM} = 1 - 0.032 \, (x - ar/2)^2,$$
$$a_{TE} = 0.722 + 0.016 \, (x - ar/2)^2 \, ,$$

where ar=5. These equations match the numerical results contained in figure 7 of reference 13 The intensity I_{22} is calculated, where both the incident and scattered light are polarized in the $x_0\text{-}z_0$ plane, and the results are shown here in figure 16.

B. THE DIELECTRIC SPHEROID

We next turn to an application where an exact calculation is available for comparison [14] We have also performed this calculation using the Shifrin method since the electrostatic polarization is known.[13] The disk method is therefore applied to the dielectric spheroid to establish its validity, and the range of validity of the first-order calculation.

The geometry is the same as used for the finite dielectric cylinder. The first-order calculation is similar to that for the cylinder except that the radius of the disks vary along the symmetry axis. The first-order contribution to the final-state electric field is

$$E^{(1)}(r) = 2\pi k_0{}^2 \exp(i \, k_0 \, r)/r$$

$$[a_{TE}(E_{oxt} \, i_t \, + E_{oyt} \, j_t) + a_{TM} \, E_{ozo} \, k_t]_{transverse}$$

$$\int dz \, a^2(z) \, J_1(q \, a(z))/(q \, a(z)) \, \exp(i \, q \, z), \tag{47}$$

where

$$a(z) = a/b \, [b^2\text{-}z^2]^{1/2} \, , \tag{48}$$

for both oblate and prolate spheroids. Here, a is the radius of the central circular cross section, and b is the half-height of the spheroid. The polarization matrix elements a_{TE} and a_{TM} are well known in the long wavelength limit and quoted in reference 13 for prolate and oblate spheroids.

The intensites I_{11} and I_{22} are defined as

$$I_{11} = (k_0 r/E_0 \,)^2 \, |E_{sc}|^2{}_{\alpha' = 90} \, .$$

$$I_{22} = (k_0 r / E_0)^2 \; |E_{sc}|^2 \quad \alpha' = 0 \tag{49}$$

where α' is the angle of incident linear polarization measured with respect to the x_0-z_0 plane. The first-order electric field is calculated using equation (27) and compared with the exact results of Asano and Yamamoto, reference 14, using a spheroid with dielectric constant $m = 1.33$, volume $V = 4.81$ μm^3, and the aspect ratio (height/diameter) 5. The wavelength of the incident light is $\lambda = 2\pi$ microns. The result for I_{22} is shown in figure 16 along with that for the comparable cylinder discussed above. It is first noted that this result for the spheroid is in excellent agreement with reference 14- as it was in reference 13. In reference 13, the Shifrin method was used to calculate the first and second order contributions to the final-state electric field. It was found that the second -order contribution is not important for this target size, wavelength, and index of refraction.

More important for the purpose of this report, this calculation shows that the decomposition of the target into disks is accurate when the disk radii vary. This allows one to approach applications that cannot be done by using the Shifrin method, nor any approach other than a brute-force evaluation of the starting integral equation, equation (25). But even for these, one needs to know the polarization matrix.

One also notes in figure 17 that the cylinder and the spheroid have distinct scattering signatures for this choice of scattering parameters.

7. APPLICATION TO DIELECTRIC TARGETS WITH A WANDERING SYMMETRY AXIS
7 A. THE DIELECTRIC HELIX

We now treat an extended target that has locally circular cross sections but whose axis is a helix. The geometry is complicated by this extension, and three frames of reference are needed to describe the scattering process. The reference frame (x_0, y_0, z_0) is as described above. The target frame (x_t, y_t, z_t) takes z_t along the helical axis. A third frame of reference (x_ϕ, y_ϕ, z_ϕ) called the disk frame is placed on a disk of infinitesimal thickness with z_ϕ through the center of the disk and perpendicular to it. This geometry is shown in the three parts of figure 17 .

The axis of the helix is traced by the vector h defined in the target frame as

$$h(\phi) = R \cos\phi \; i_t + R \sin\phi \; j_t + P/(2\pi) \phi \; k_t \tag{50}$$

Here, R is the radius of the helix, P is the pitch, and ϕ is the angular variable that is shown in the figures18. The + and - signs define right- and left-handed helicity, respectively. Note that ϕ runs from 0 at one end of the helix (at the origin) to $2\pi n$ (n= number of turns) at the other end.

The vector $h(\phi)$ marks the position of the center of a disk. The disk z axis is along the differential vector

$$dz = dh/d\phi \; d\phi$$
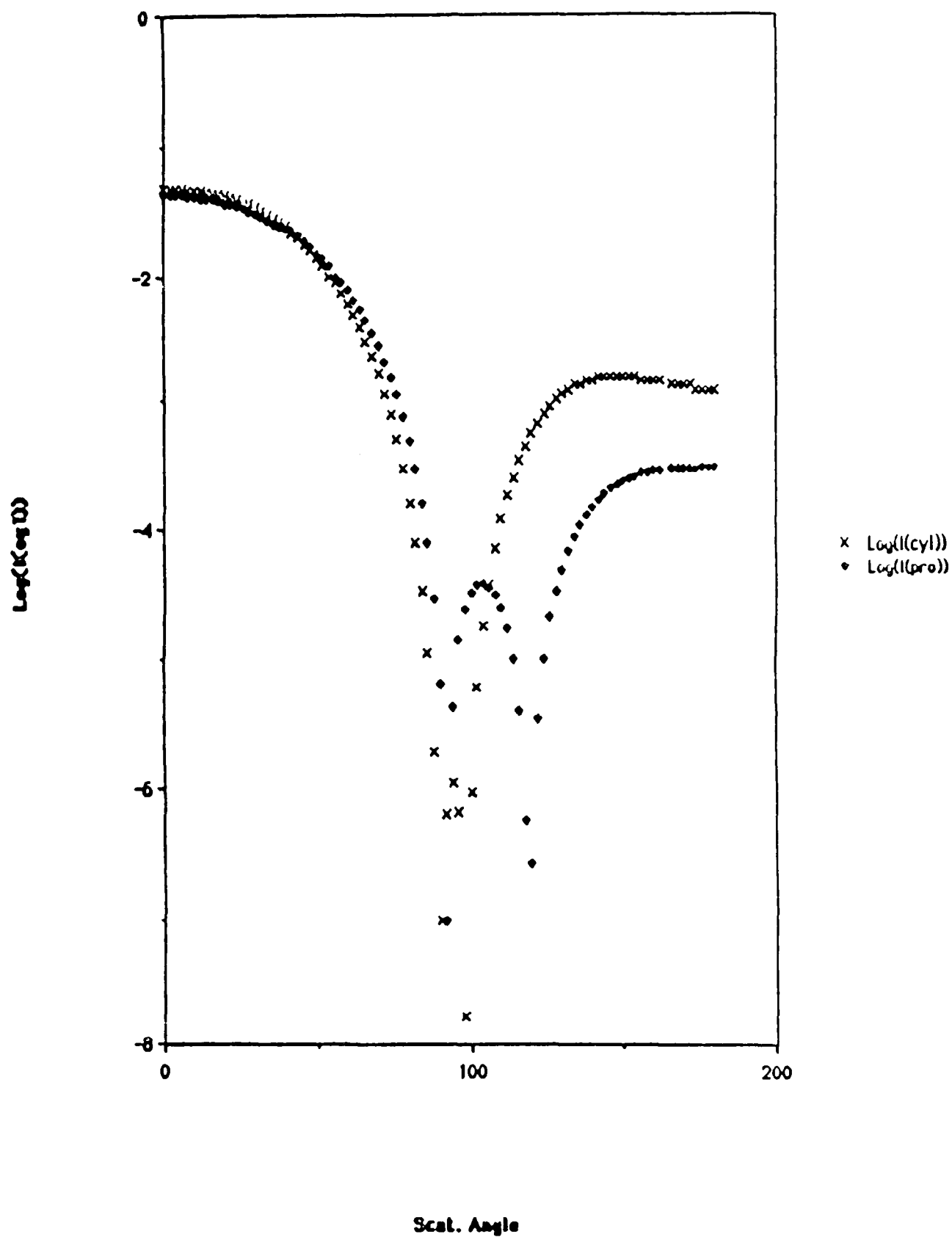$$= \{-R(\sin\phi \; i_t - \cos\phi \; j_t) + P/(2\pi) \; k_t \} \; d\phi. \tag{51}$$

Figure 16. The intensity I_{22} is shown for a cylinder and prolate spheroid of index m = 1.33, aspect ratio 5 and volume 4.8 μm^3. This intensity corresponds to the case when both the incident and the scattered light are linearly polarized in the scattering plane. The polarization matrix for the cylinder varies as described in the text.
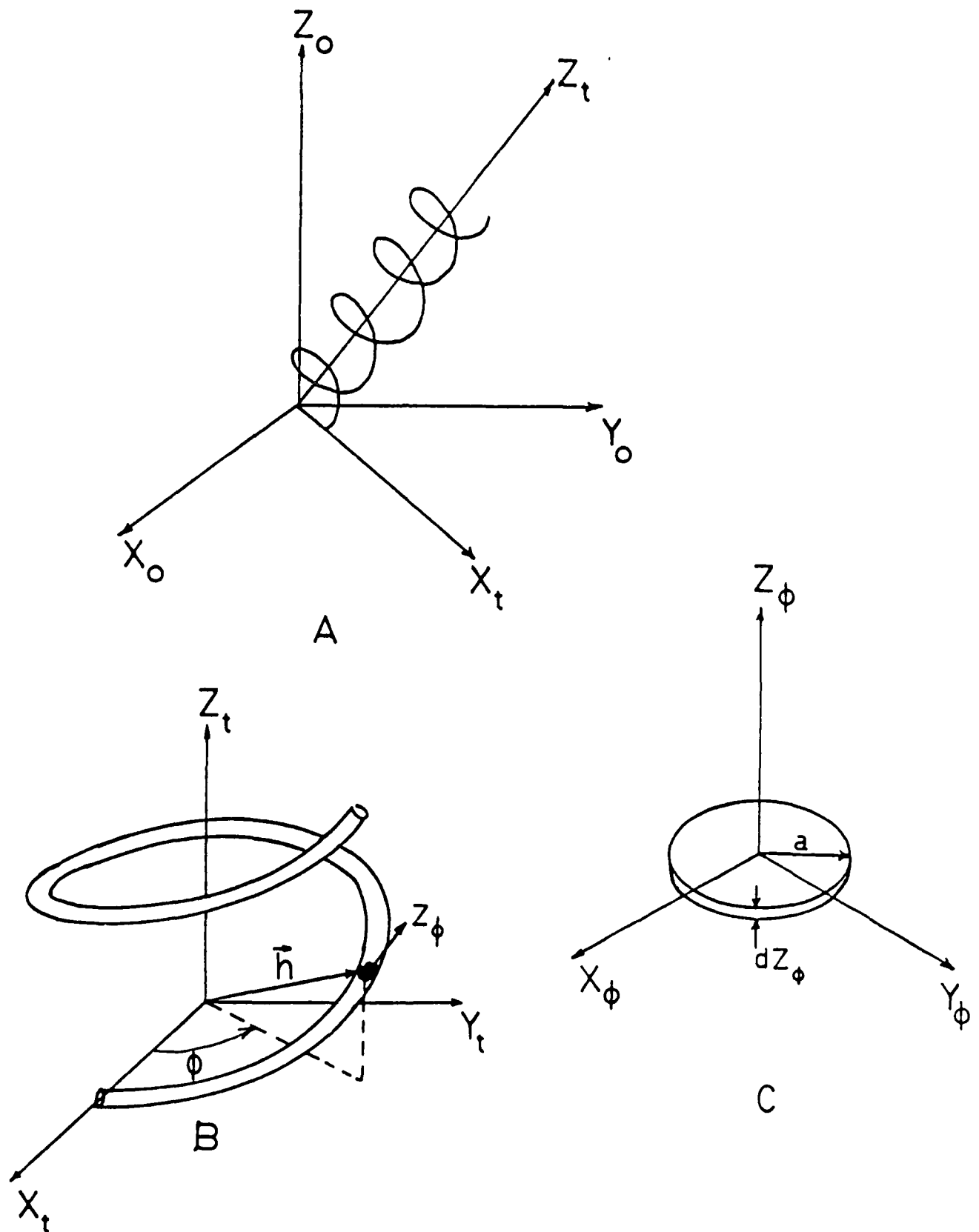
38

Figure 17. A) The reference and target frames of reference shown for a helical target. B) A detailed view of the helix in the target frame of reference. An infinitesimal disk is shown located by the vector **h**(φ) with azimuthal angle φ. C) A detailed view of a disk in the disk frame of reference. The disk radius is denoted a.

The magnitude of dz_ϕ is independent of ϕ and given by

$$dz = [R^2 + (P/2\pi)^2]^{1/2} d\phi. \tag{52}$$

The unit vectors for the disk frame are chosen as

$$k = \{-R (\sin\phi\, i_t - \cos\phi\, j_t) + (P/2\pi) k_t\} /S ,$$

$$i = \cos\phi\, i_t + \sin\phi\, j_t ,$$

$$j = k \times i = \{+ (P/2\pi) (\cos\phi\, j_t - \sin\phi\, i_t) - R\, k_t\} /S,$$

$$S = [R^2 + (P/2\pi)^2]^{1/2}. \tag{53}$$

The transformation from the reference to the disk frame is achieved through the orthogonal transformation

$$X_{\phi,i} = (T_{t \rightarrow \phi})_{ij} (T_{0 \rightarrow t})_{jk} X_{0,k} = (T_{0 \rightarrow \phi})_{ik} X_{0,k}. \tag{54}$$

The transformation matrix is given in the appendix of reference Note that this transformation is unitary,

$$T_{\phi \rightarrow 0} = T_{0 \rightarrow \phi} \quad .$$

Our model assumes that the polarization matrix A, appearing in equation (1), is constant and diagonal in the disk frame of reference, with the x_ϕ and y_ϕ matrix elements equal due to the cylindrical symmetry. To take advantage of this assumption, each term in the integrand of equation (15) must be expressed in the target frame and then transformed to the reference frame. The first-order contribution to the field is therefore given by:

$$E_i^{(1)}(r) = 2\pi \exp(ik_0 r)/r\, k_0^2 \int S\, d\phi\, a^2 J_1(q(\phi) a)/(q(\phi) a)$$

$$\exp(iq(\phi) h(\phi))\, (T_{\phi \rightarrow 0})_{ij}\, \{[A_{jl} - r_j r_k A_{kl}]\, E_{0,l}(\phi)\}_{disk}, \tag{55}$$

where n is the number of turns in the helix. The transformation matrix $T_{f \rightarrow 0}$ is introduced in equation 54 and specified in the appendix of reference Here, a is the radius of each disk (wire radius) and $q = k_0 (r - k_0)$, r is a unit vector directed from the origin of the target frame to the field point (the far-field approximation is used) and k_0 is a unit vector in the direction of the incident light. Thus, it is necessary to continuously transform from the disk to the reference frame as the integration over the helix is performed. Therefore, the scattering effects from the disks that compose the target are added

coherently, their phases being matched by the exponential factor in the integrand of (55). Moreover, the vector q appearing in the Bessel function is the magnitude of the vector q perpendicular to the local disk axis. We get this quantity by using the transformation of equation (54):

$$\begin{vmatrix} q_x \\ q_y \\ q_z \end{vmatrix} = T \begin{vmatrix} k_0 \sin(2\phi_0) \\ 0 \\ k_0 \cos(2\phi_0) \end{vmatrix} \tag{56}$$

where $2\phi_0$ is the scattering angle. It follows that

$$q(\phi) = [(q\, i_\phi)^2 + (q\, i_\phi)^2]^{1/2}$$

$$= \{(\cos\phi\, q_{xt} + \sin\phi\, q_{yt})^2 +$$

$$(-R\, q_{zt} + (P/2\pi)(\cos\phi\, q_{yt} - \sin\phi\, q_{xt})^2 / S^2\}^{1/2} \tag{57}$$

The phase term in equation (35) has the exponent

$$q\, h = R\cos\phi\, q_x + R\sin\phi\, q_y + (P/2\pi)\,\phi\, q_z \ . \tag{58}$$

The last factor in equation (35) contains the components of the incident field in the disk frame; therefore, the incident electric field, normal to k_0, must be transformed as

$$\begin{vmatrix} E_{ox\phi} \\ E_{oy\phi} \\ E_{oz\phi} \end{vmatrix} = T_{0\to\phi} \begin{vmatrix} E_{ox} \\ E_{oy} \\ 0 \end{vmatrix} \tag{59}$$

7 B. CALCULATION OF THE CIDS FOR THE DIELECTRIC HELIX

The scattering of light from very thin helical targets has been discussed by various authors[15-18] where the helix is treated essentially as a line of dipoles set on the helical axis. Singham, Patterson, and Salzman, reference 19, have also considered light scattering from chiral objects, including the helix, using a model that descibes the three-dimensional body as a collection of spherical or ellipsoidal dipoles. The quantity of special interest in these papers is called the circular intensity differential scattering parameter (CIDS) defined as

$$CIDS = (I_L - I_R)/(I_L + I_R) \ . \tag{60}$$

Here I_L is the scattering intensity for left-circularly polarized light

41

$$E_0 = E_0 \, (i_0 \pm i \, j_0),$$

with the upper and lower signs corresponding to right and left circularly polarized light, respectively (with the time factor $i\omega t$). In the series of papers by Bustamante and others, refs. 16-18 , the CIDS parameter is evaluated for very thin wires for which, in our notation, $a_{TE} = 0$ and $a_{TM} = 1$. In reference 16, a series of calculations is performed for a helix with n= 20, R=1μm , p = 1 μm, and for wavelengths from 1 μm to 4μm. The spiral axis is located at

$$o_t = 90 \quad \text{and} \quad \gamma_t = 90 \quad .$$

We have calculated the CIDS ratio for the helix described above for the wavelengths 1,2, 4, and 6 μm. It should be emphasized that our model is different than that of Bustamante. Our helices have thickness and are dielectrics of refractive index 1.5. The polarization matrix is diagonal and of the form of equation (22) with $a_{TE} = 2/(m^2 + 1)$ and $a_{TM} = 1$ in each disk frame of reference. In general, we find that our results give about the same signatures as those of Bustamante et al., that is the number, size, and placement of the lobes are about the same as found by them. However, we do not get their large back- attering lobes . Figure 18 is a polar plot of the CIDS ratio, where 1 = 1 μm. Figure 19 is similar b ith 1 = 2μm. In figure 20, we attempt to match the Bustamante calculation by taking m=50 w ich makes a_{TE} small (note that the radius is correspondingly small so that the condition $2\pi a m / \lambda < 2$ is satisfied). After doing this we get a large backscattering lobe. figure 21 is a CIDS plot for 1 = 4 μm, m=1.5 , and only one prominant lobe is present, and again this is consistent with reference 16. Figure 22 is calculated as in figure. 6 but with 1 = 4 μm , and a backscattering lobe again appears. Figure 23 is a CIDS plot for a wavelength 1 = 6 μm. Here there is one very wide lobe with a large backscattering contribution even though the calculation is for a thin dielectric.

It should be pointed out that o results for a thin dielectric differ from the results of reference 16 even when the radius of the wire is to be very thin, a = 0.0001 μm, and, in fact, CIDS does not change significantly for radii from thi e to about 0.1 μm. Thus, a thin dielectric wire is not the same as a train of dipoles placed along t al axis . Any finite thickness seems to make a difference, especially in the back scattering range. 1 sult seems to be borne out by the work of reference 18 , where it is found that triaxial polarizabili (which are related to differing diagonal matrix elements of the polarization matrix) significantl affect the scattering result and therefore have to be included to qualitatively describe the scattering matrix. The model of reference 18 , though not treating the target as being a continuous body as does our model, is nevertheless three dimensional and thus closer to our treatment than the one dimensional model of reference 16.

One final calculation is made, based on an electron micrograph of Spirillum membranes presented in reference 16 These researchers use the following scattering parameters for this application: $\lambda = 260$ nm, pitch = 2.6 nm, radius of helix = 208 nm, and 6 turns. Our calculation uses a real index of
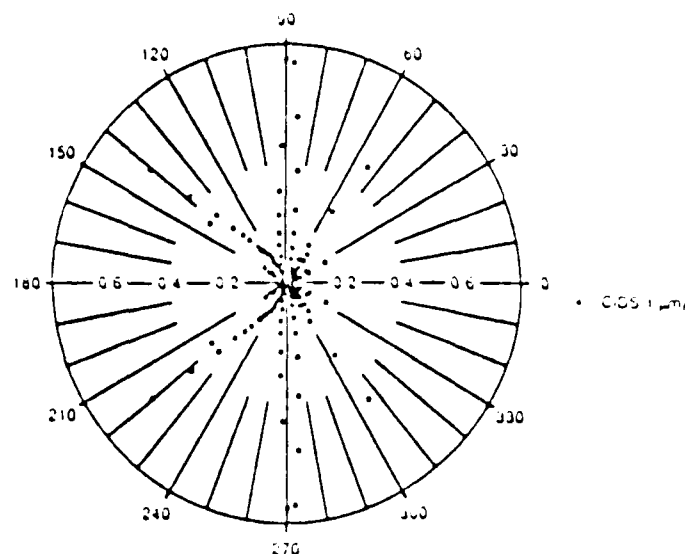
Figure 18. The CIDS parameter defined in equation 60. The target is a dielectric helix of index of refraction m = 1.5. The helix is formed from a thin cylinder of radius a = 0.01 μm. The helical radius is R = 1 μm, the pitch is P = 1 μm, and the helix is right handed with 20 turns. The wavelength of the incident light is 1 μm. The polarization matrix is assumed to be diagonal in the frame of reference of each disk, and the values of its elements within each disk are $a_{TE} = 2/(m^2+1)$ and $a_{TM} = 1$. These values are the same as for an infinite dielectric cylinder in an electrostatic field.
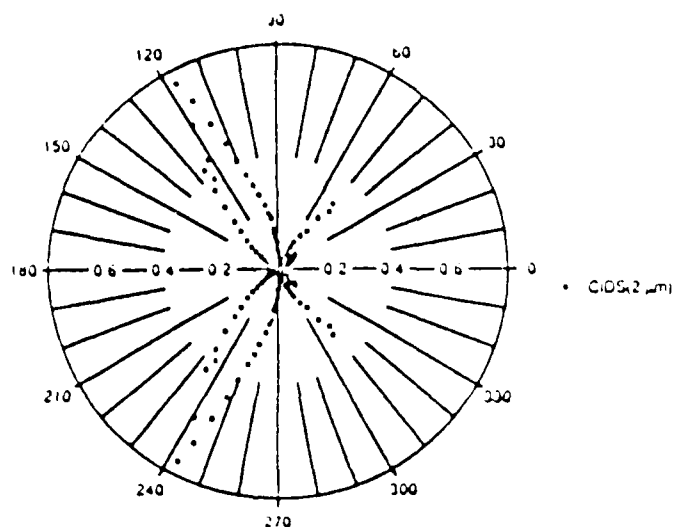
Figure 19. The CIDS parameter for the same helix and the same polarization matrix as in figure 18. The incident light has the wavelength 2μm.

43
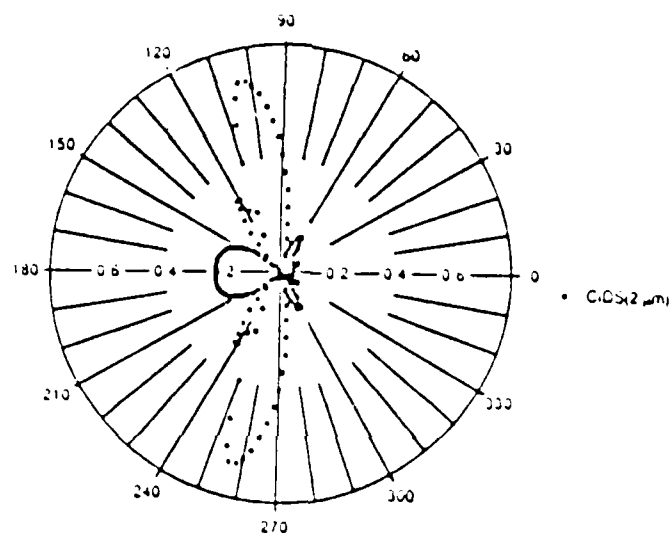
Figure 20. The CIDS parameter for the same helix as in figure 18, and the wavelength of the incident light is again 2 μm. However, to simulate a helix constructed of an infinitely thin wire with $a_{TE} = 0$, we take m = 50 and the radius a = 0.001.

44
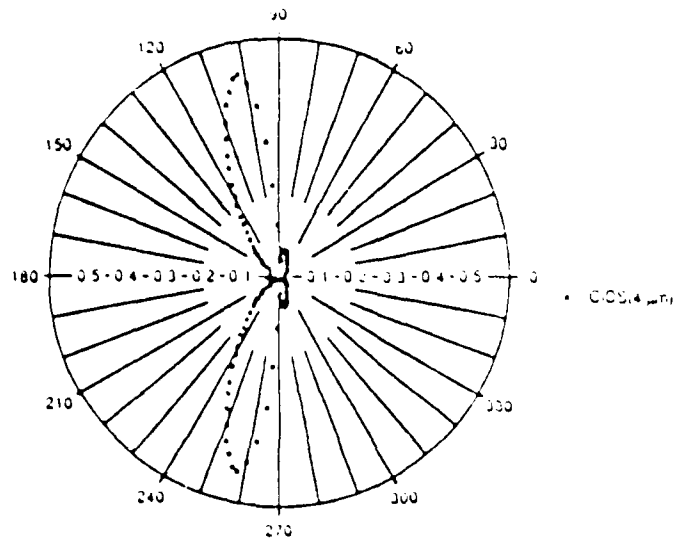
Figure 21. The CIDS parameter for the samd helix as in figure 18. The wavelength of light is 4 μm, and the polarization matrix elements for each disk are the same as described in figure 18.
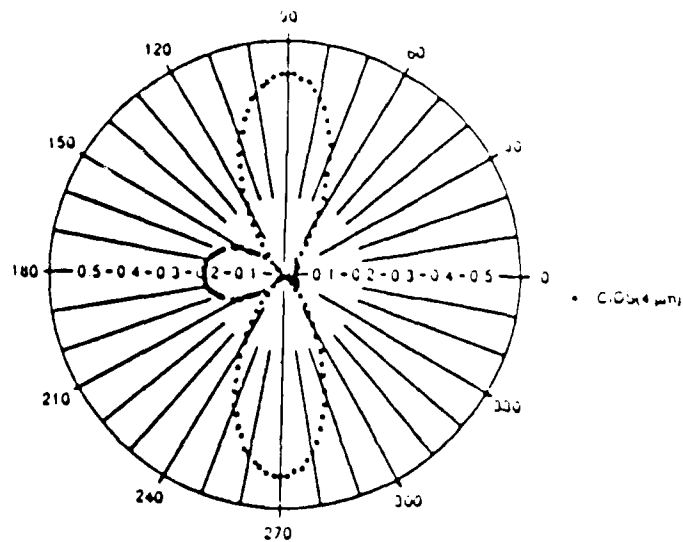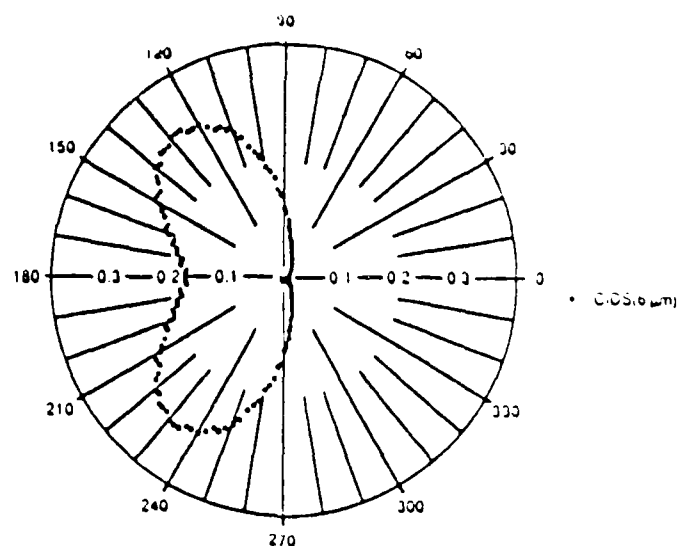

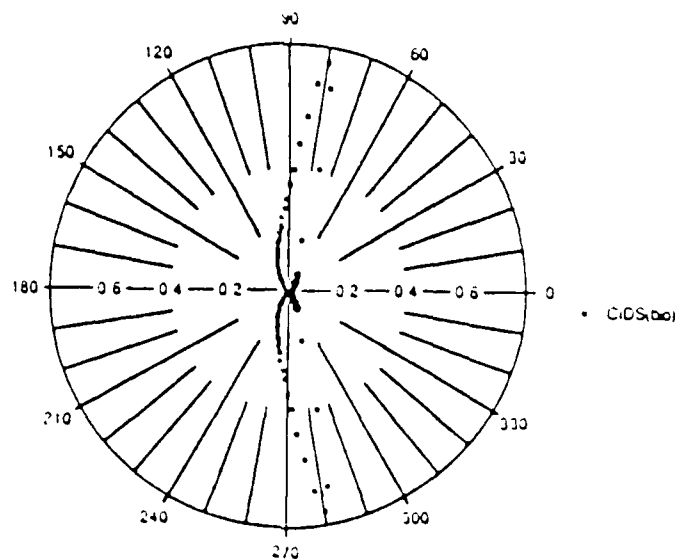Figure 22. The CIDS parameter for the same helix and incident light as in figure 21, but modified as in figure 20.

Figure 23. The CIDS parameter for the same helix as in figure 18. The wavelength of the incident light is 6 μm, and the polarization matrix elements for each disk are as described in figure 18.

Figure 24. The CIDS parameter for a biologically- modelled helix. The index of refraction is taken to be m = 1.33. This helix has 6 turns, and its size parameter and wavelength of the incident light are given in the text. The polarization matrix for each disk is as described in figure 18.

46

refraction of 1.33, and our results are shown in figure 24. The results of reference 26 ... application show two lobes with almost the same maximum for the CIDS parameter, about ... Our results indicate a thinner lobe with the same maximum value occuring at about the same scattering angle of 8θ.

7 C . DIELECTRIC TOROID.

The helix reduces to a toroid when the pitch $p = 0$. Therefore, the evaluation of the electric field proceeds as for the helix. For a dielectric toroid with volume $V = 4.8 \, \mu m^3$, the intensity I_{22} is calculated for two wavelengths, $\lambda = \pi \, \mu m$ and $2\pi \, \mu m$. This target size insures that the first order contribution is accurate by virtue of our work in reference 13.

The scattering intensity I_{22} is calculated and compared to an oblate spheroid of the same volume and aspect ratio 1/5. The index of refraction of both targets is $m = 1.33$, and the toroid has $a = 0.358 \, \mu m$, $R = 1.9 \, \mu m$. The oblate spheroid has a radius $1.79 \, \mu m$ and a height $0.716 \, \mu m$. Again, each shape has the same volume. The results are shown in figures 25 and 26. Figure 25 shows quite different signatures for the two shapes when the wavelength is $\pi \, \mu m$, the toroid alone has a minimum at about a scattering angle of 40 degrees, and the backscattering intensity for the toroid is appreciably larger than for the spheroid (note that this is a log plot, so the difference in backscattering intensities is almost two orders of magnitude). In figure 26, with $\lambda = 2\pi \, \mu m$, these differences are nearly eliminated - the only real difference between the patterns being the central minima occuring at slightly different scattering angles.

8. SCATTERING OF LIGHT FROM A DIELECTRIC HELIX - EXPERIMENT

Experimental studies of scattering by a single particle are very difficult to perform in the optical region, especially when the particle size is comparable to the wavelength of the incident radiation. The considerable advantages of using the microwave analog technique in simulating single particle scattering have been described elsewhere.[8-10]We select here some recent angular distribution measurement results for a dielectric helix employing this technique.

A right handed, 7-turn helix of 3.66 cm outer diameter and of 4.35 cm axial length was formed from a 0.48 cm diameter plexiglass cylinder, a commercially available acrylic rod. The complex dielectric constant of this plastic material was separately measured by a classical standing wave technique using a waveguide-slotted-line, from which the complex refractive index was found to be $m = 1.626 - 0.012 i$ at the operating microwave wavelength $\lambda = 3.18$ cm.

The microwave-unique compensation (or null) technique was employed in both extinction $(2\theta_0 = 0^\circ)$ and in angular scattering $(10^\circ < 2\theta_0 < 170^\circ)$ intensity measurements, and from the former, one can also deduce the scattering intensity in the beam direction $(2\theta_0 = 0^\circ)$. Presently, the null technique is the only reliable method with which one can discriminate the true scattered wave against the superimposed, yet unwanted coherent background radiation, whose magnitude may be comparable to or even much
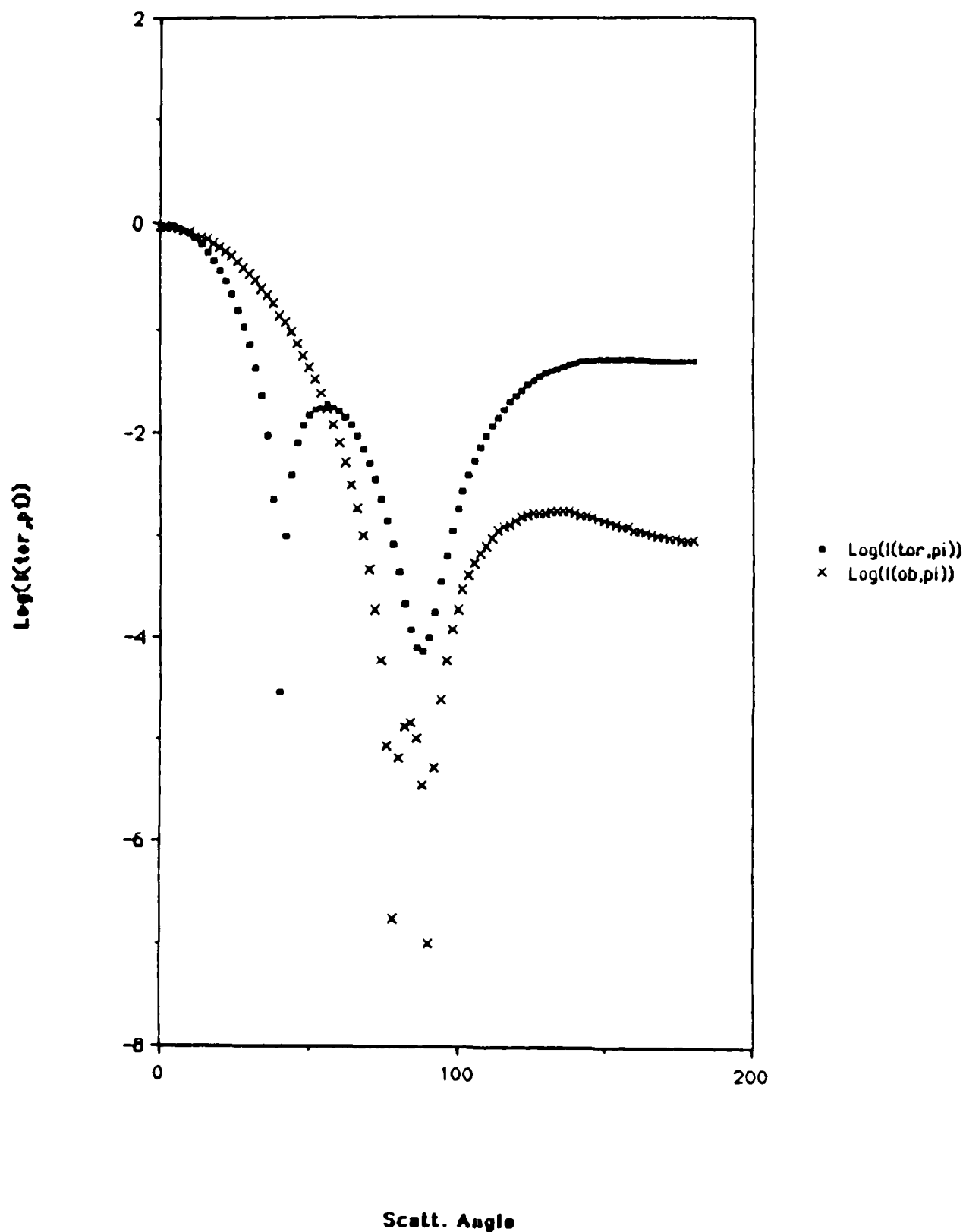
Figure 25. The intensity I_{ss} for a dielectric toroid and an oblate spheroid. The volume of each target is $4.8 \mu m^3$ and the index of each is $m = 1.33$. The other size parameters are given in the text. The wavelength of the incident light is $\pi \mu m$.
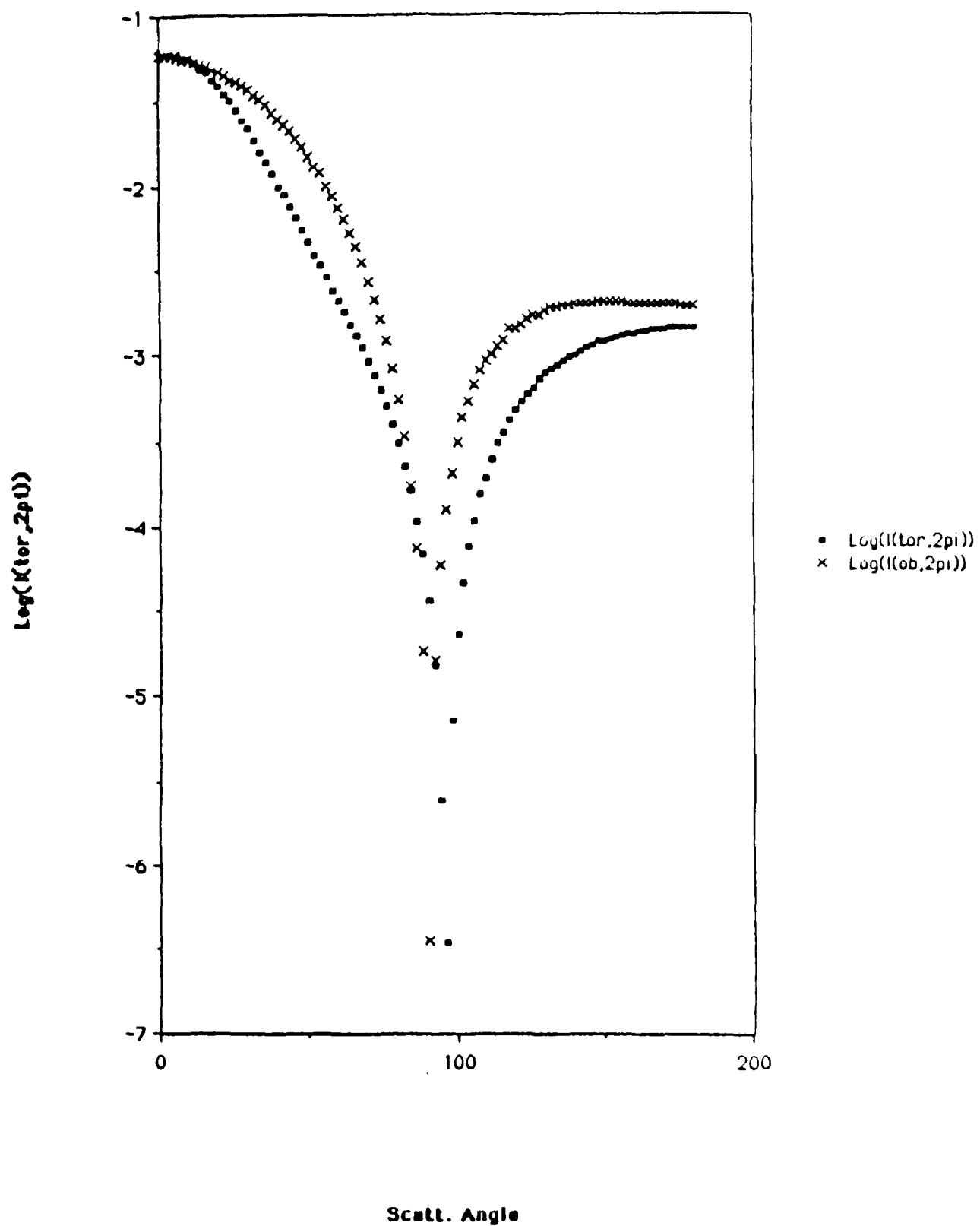
Figure 26. The intensity $I_{??}$ for the same dielectric toroid and oblate spheroid as in figure 25. In this case, the incident light has the wavelength 2π cm.

larger than the former.

A brief explanation of measurement procedures using this technique is needed. In the absence of the target in the beam, one cancels the unwanted background at the output port of a mixer by properly adjusting both the amplitude and the phase of a reference wave which is piped through a separate waveguide from the microwave source to an input port of the mixer, while the background wave via free space is being fed to the other mixer input port. As the target is hoisted into the beam, the off-balance appearing in the mixer port is directly proportional to the true scattered wave. The target is thereby allowed to go through a preselected sequence of orientations in the beam, and the orientation-dependent data are recorded. Immediately after the run, the target is replaced by a standard target of known scattering magnitudes, and the measured scattering of this standard provides the absolute magnitude calibration of the entire run. Therefore, it follows that the accuracy of the scattering experiment hinges most critically on the stability of cancellation, i.e., on how long the initially established null condition is maintained. Any disturbance affecting the initial cancellation will apperar as drift or noise in the detected signal, which is virtually impossible to correct after the measurement is made. It also follows that the measurement accuracy degrades as the scattered signal level becomes lower in comparison to the drifting background or reference wave.

The measured scattering intensities (in absolute magnitude) are denoted I_{11} and I_{22}. The intensity I_{11} is the case when both the receiving and transmitting antennas are polarized vertically, I_{22} is for both antennnas polarized horizontally. The horizontal scattering plane corresponds to the x_0-z_0 plane in figure 27. Inspection of the experimental profiles I_{11} and I_{22} (figures 28,29,30) versus the scattering angle $2\theta_0$ immediately shows that the scattering by the helical structure is hightly sensitive to the orientation of the helix in the beam; and also that the intensity may vary as much as four orders of magnitude (figure 28) as the scattering angle changes. Because of the rather small size of the helix compared to the large antenna-target separations (10.8 m between the transmitter and target; 5.2 m between receiver and target), and hence the low scattered signal levels, significant measurement errors may exist due to the afore-mentioned compensation stability. Roughly estimated, the cumulative maximum errors would be about 5% if the absolute magnitudes of I_{11} and I_{22} are larger than 10^1, up to approximately 20 % for those between 10^0 and 10^1, and may amount to as much as 100 % for those magnitudes having less than 10^{-1}. Also, the system gain changes during the lengthy measurement runs may have contributed additional absolute-magnitude-calibration errors. Roughly estimated, the cumulative maximum errors would be about 5% if the absolute magnitudes of I_{11} and I_{22} are larger than 10^1, up to approximately 20 % for those between 10^0 and 10^1, and may amount to as much as 100% for those absolute magnitudes having less than 10^{-1}.

9 COMPARISON OF THEORY AND EXPERIMENT

The series of measurements on the scattering of microwaves from a dielectric spiral target have been performed, as described above, and theoretical calculations are compared with the intensities I_{11} and
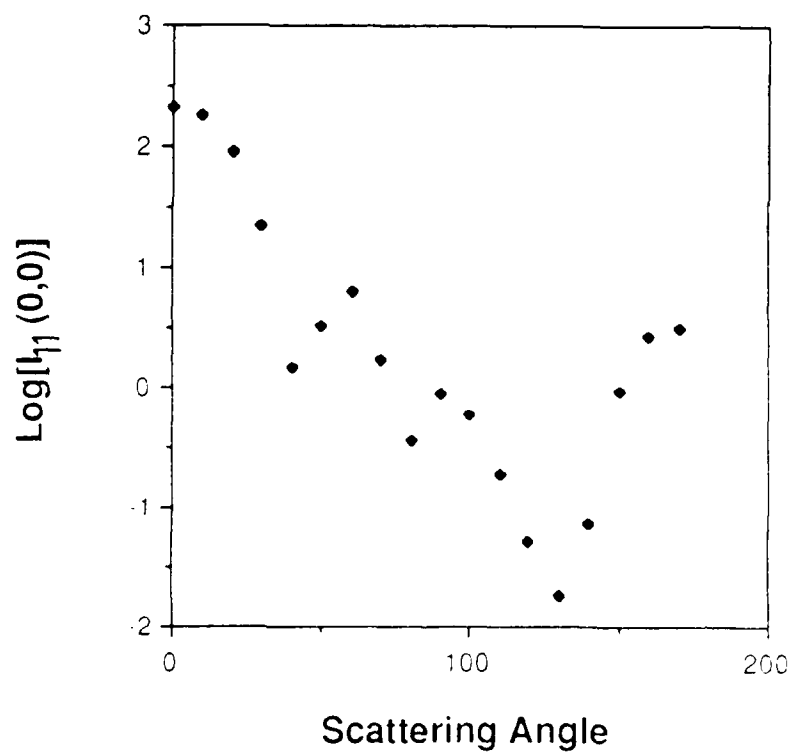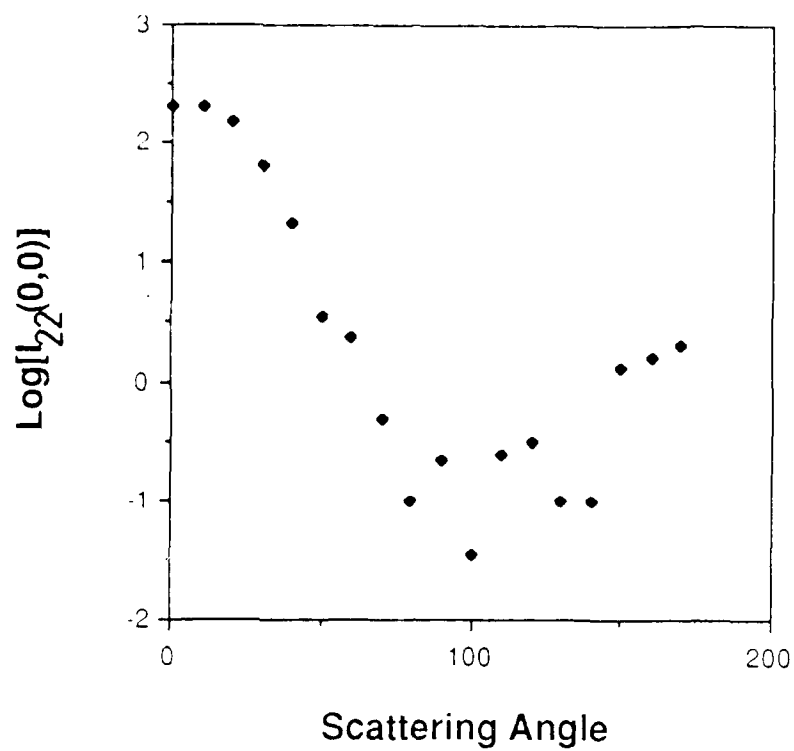
Figure 27. a) The reference frame, where z_o is in the direction of incident light. r is the direction of scattered light, and x_o is in the scattering plane formed by z_o and r. The axis of the helix is along z_t whose orientation angles are ϕ_t and γ_t. The incident electric field direction is E_0 and it makes an angle β with the scattering plane. The scattering angle is $2\phi_o$.
b) The helix shown in the reference frame. The helix is oriented at angles determined by γ_t and z_t.
c) Detailed drawing of the helix. [illegible] which indicates the axis of the helix.

51

Figure 28. Experimental scattering profiles $I_{11}(0,0)$, $I_{22}(0,0)$ versus scattering angle $2\Phi_0$.
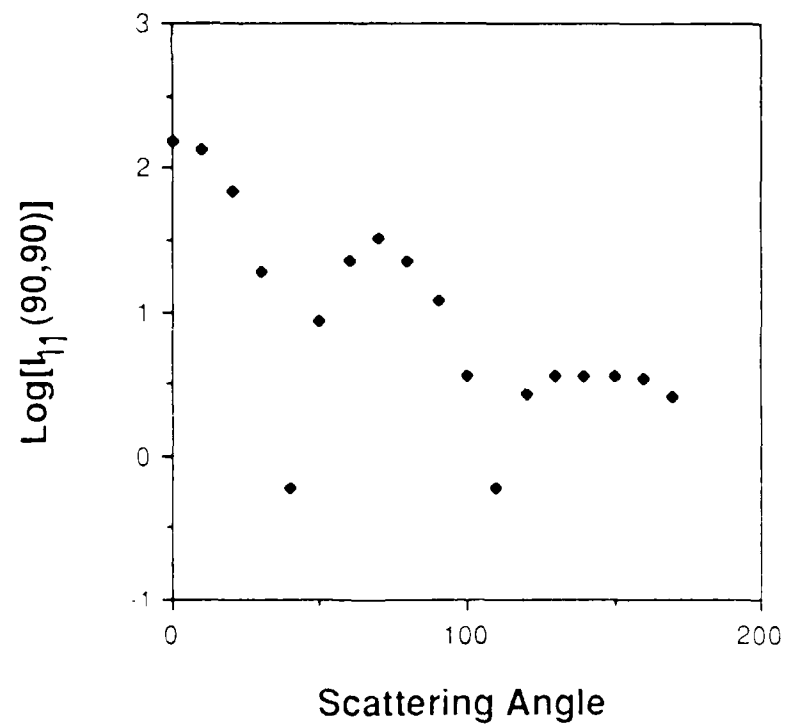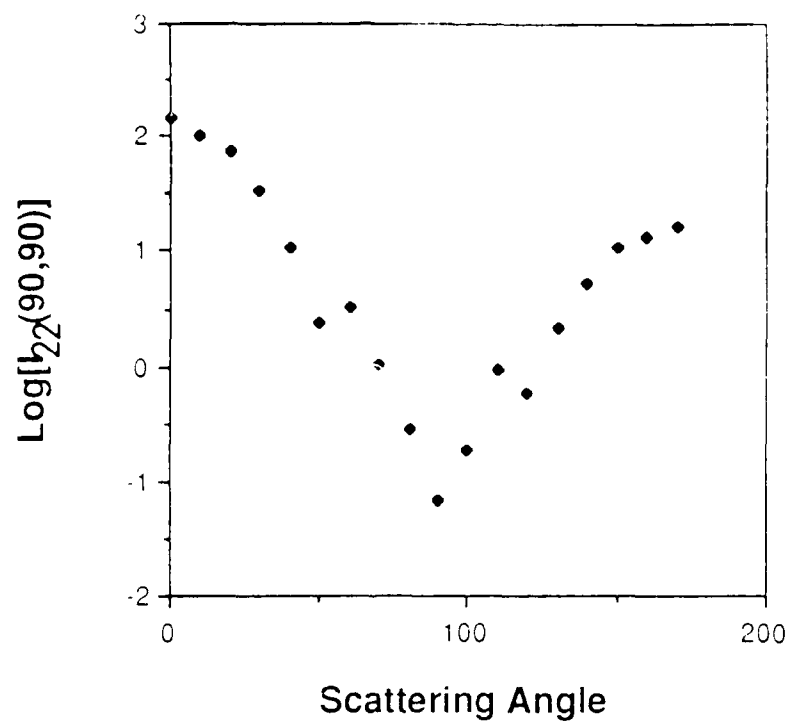
Figure 29. Experimental scattering profiles $I_{11}(90,0)$, $I_{22}(90,0)$ versus scattering angle $2\phi_0$.
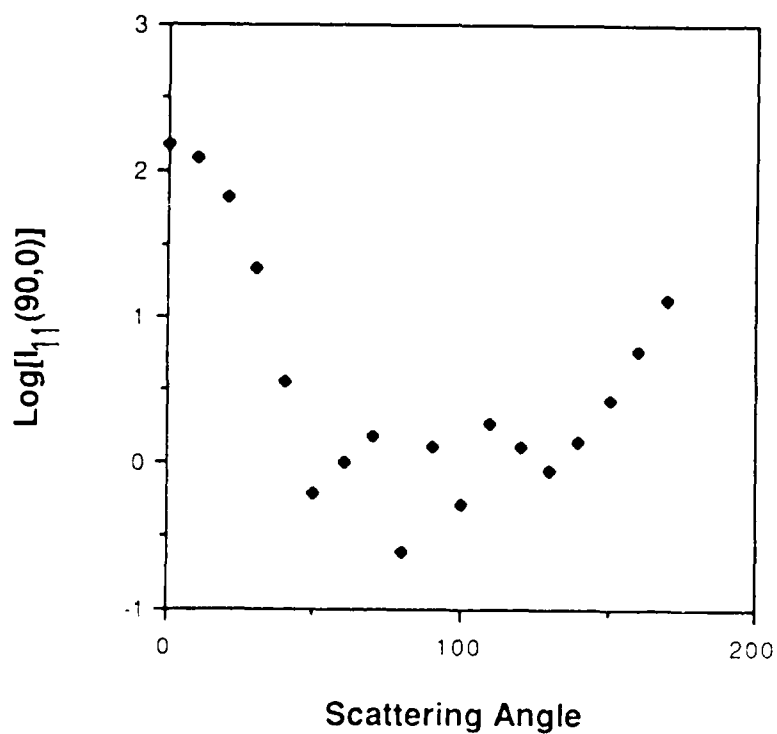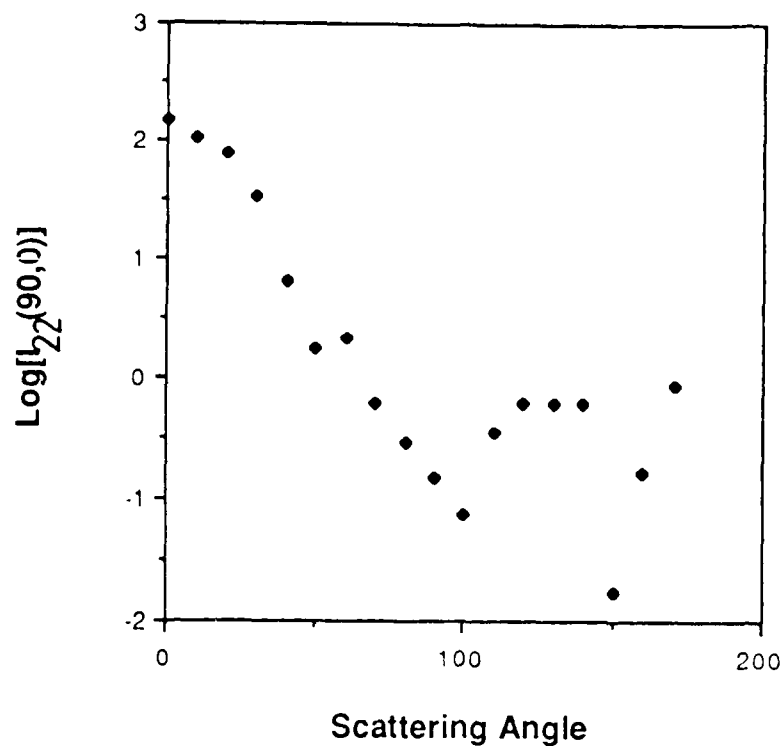
Figure 30. Experimental scattering profiles $I_{11}(90,90)$, $I_{22}(90,90)$ versus scattering angle $2\phi_0$.

I_{22} for which the plane of polarization is not changed by the scattering.

The range of parameters for the helix used in these experiments are in the range of applicability of the integral method for calculating scattering intensities. The intensities calculated are I_{11}, where the directions of initial and final linear polarization are perpendicular to the scattering plane, and I_{22}, where the directions of linear polarization are in the scattering plane (the scattering plane is formed by the directions of incidence and scattering - the x_0-z_0 plane of the theoretical discussion).

The experimental results for $I_{11}(0,0)$, $I_{22}(0,0)$ are shown in figures 28, the results for $I_{11}(90,0)$ and $I_{22}(90,0)$ are shown in figures 29, and the results for $I_{11}(90,90)$ and $I_{22}(90,90)$ are shown in figures 30. Here, for example $I_{11}(90,0)$ corresponds to the helix orientation $\theta_t = 90$ and $\gamma = 0$. Note that the values never drop to below 10^{-2}, even though the theory predicts minima that are far smaller. We account for this by noting that the real target is not perfectly shaped, and hence the very sharp minima produced by an ideal spiral would not be expected. Moreover, the noise level inherent in the experiment prohibits meaningful measurements three orders of magnitude below maximum values. The positions of the minima are of greatest importance as these are produced by the spiral geometry, and we summarized these minima for the experiments from figures 28 as best we can as

$$I_{22}(0,0) : \; 50°, 75°, 100°, 140°;$$
$$I_{11}(0,0) : \; 40°, 70°, 135°,$$

for figures. 29 as

$$I_{22}(90,0): 50°, 70°, 90°, 150°;$$
$$I_{11}(90,0): 50°, 70°, 105°, 140°;$$

and for figures. 30 as

$$I_{11}(90,90): 45°, 115°;$$
$$I_{22}(90,90): 55°, 90°, 125°.$$

figures 31 through 36 contain the intensities $I_{11}(0,0)$, $I_{22}(0,0)$, $I_{11}(90,0)$, $I_{22}(90,0)$, $I_{11}(90,90)$, and $I_{22}(90,90)$ and the comparison of the theory and experiment. The experimental points are shown as solid diamonds while the theoretical results are plotted as a line.

The comparison between theory and experiment is evident from the figures in which the theoretical results are normalized with the experiment at the smallest scattering angle (10). We can summarize this comparison as follows:

(1) Reasonably good agreement between theory and experiment for forward and back scattering. The forward to back-scattering ratios are particularly well established by the theory for the intensities $I_{22}(0,0)$, $I_{11}(90,0)$, and $I_{22}(90,90)$.

(2) Good agreement between theoretical and experimental values for the I_{11} intensities. The structure of the intensity patterns for $I_{11}(0,0)$ and $I_{11}(90,90)$ is particularly striking, and the good agreement occurs where the both theoretical and experimental value are within two orders of magnitude of the forward scattering values. In general, agreement is best where the theoretical values do not descend below about two or three orders of magnitude of the forward values. This result is reasonable

since the experimental values have large uncertainties for such small intensities as described above.

(3) The positions of most of the experimental minima generally agree well with the theory.

One concludes that the theory presented here explains the general features of the spiral experiment. Since the theory can be applied to a wide range of particle shapes, this technique provides a method by which such target shapes can be studied without resorting to time- consuming numerical procedures.
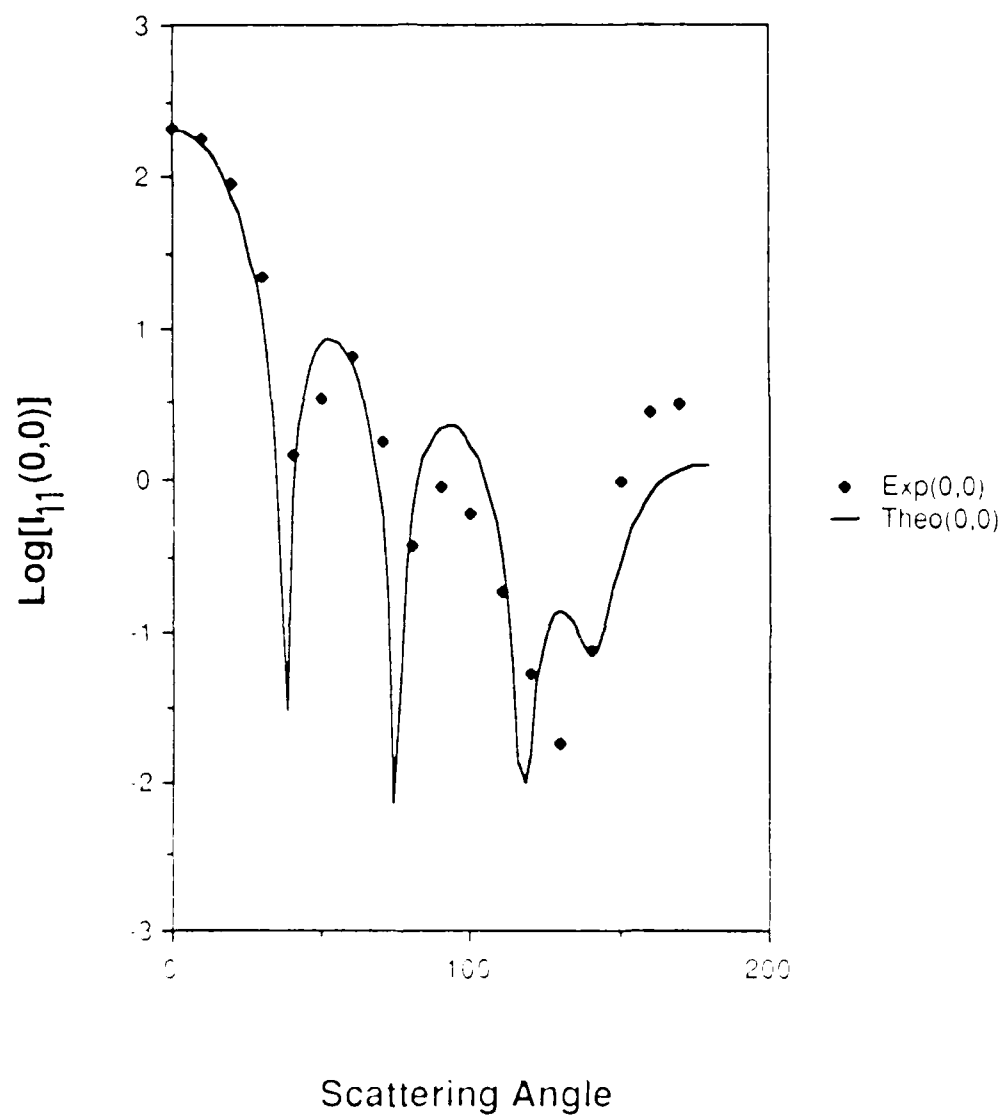
Figure 31. A comparison between theory and experiment for the $\log(I_{11})$ plotted against the scattering angle $2\theta_0$ for the orientation $\phi_i = 0$ and $\gamma_i = 0$.
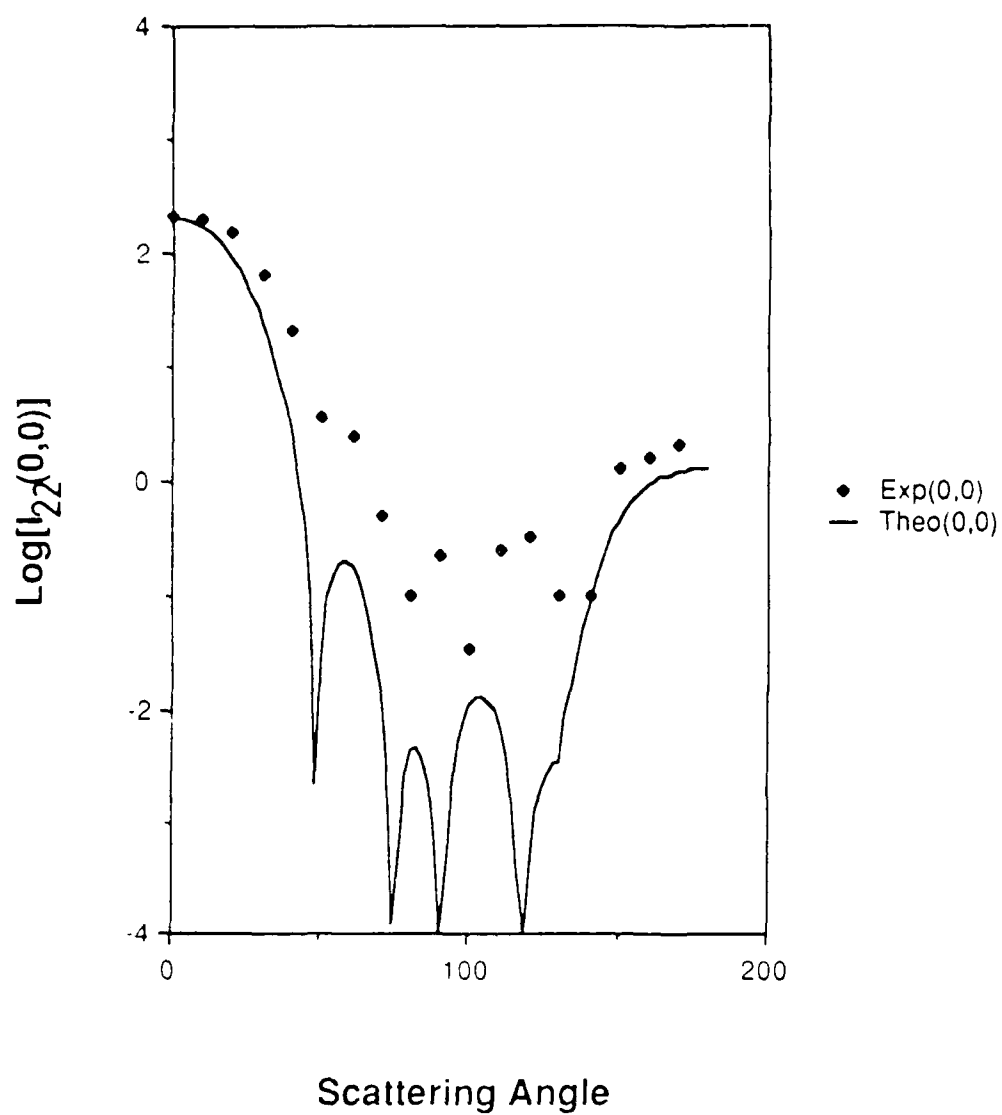
Figure 32. A comparison between theory and experiment for the log(I_{22}) plotted against the scattering angle $2\phi_0$ for the orientation $\phi_t = 0$ and $\gamma_t = 0$.
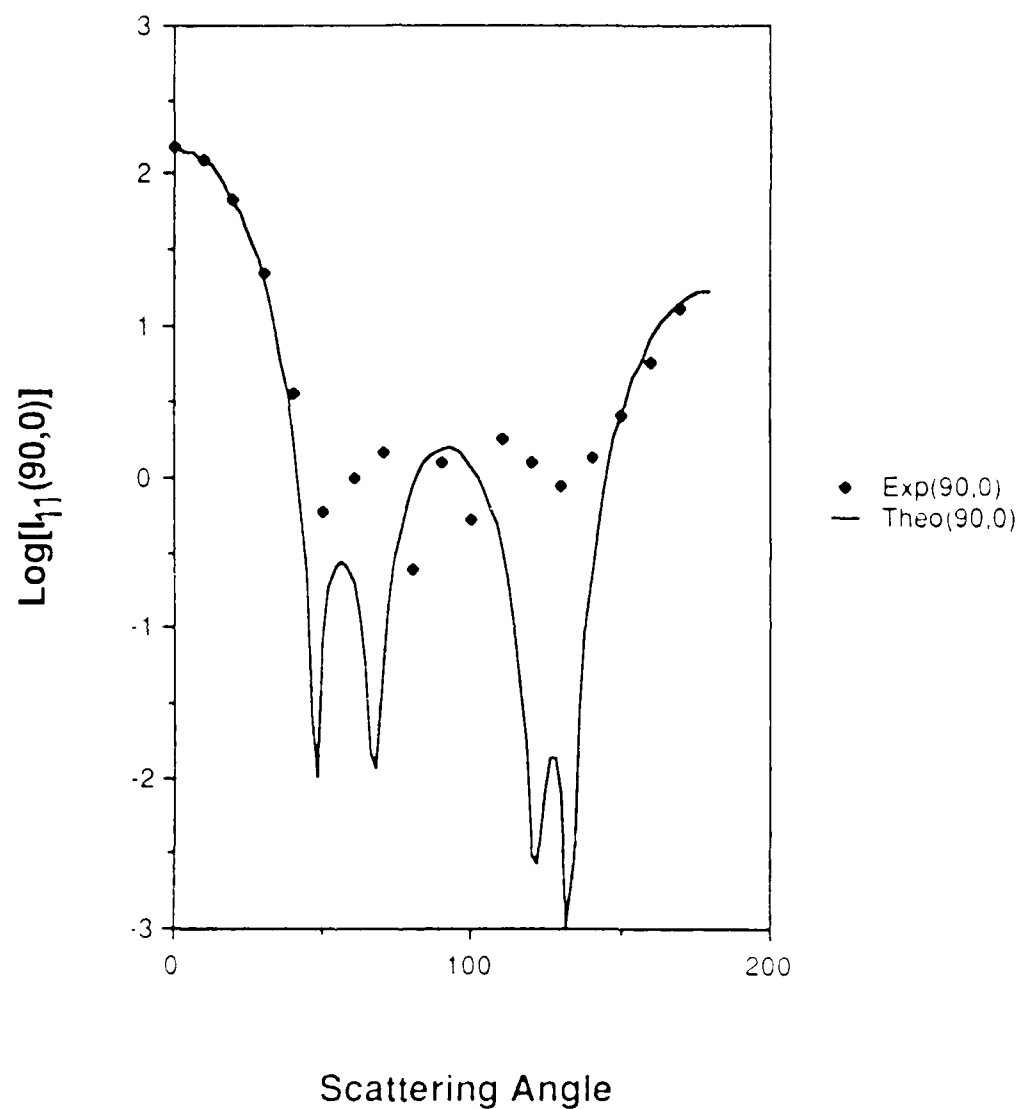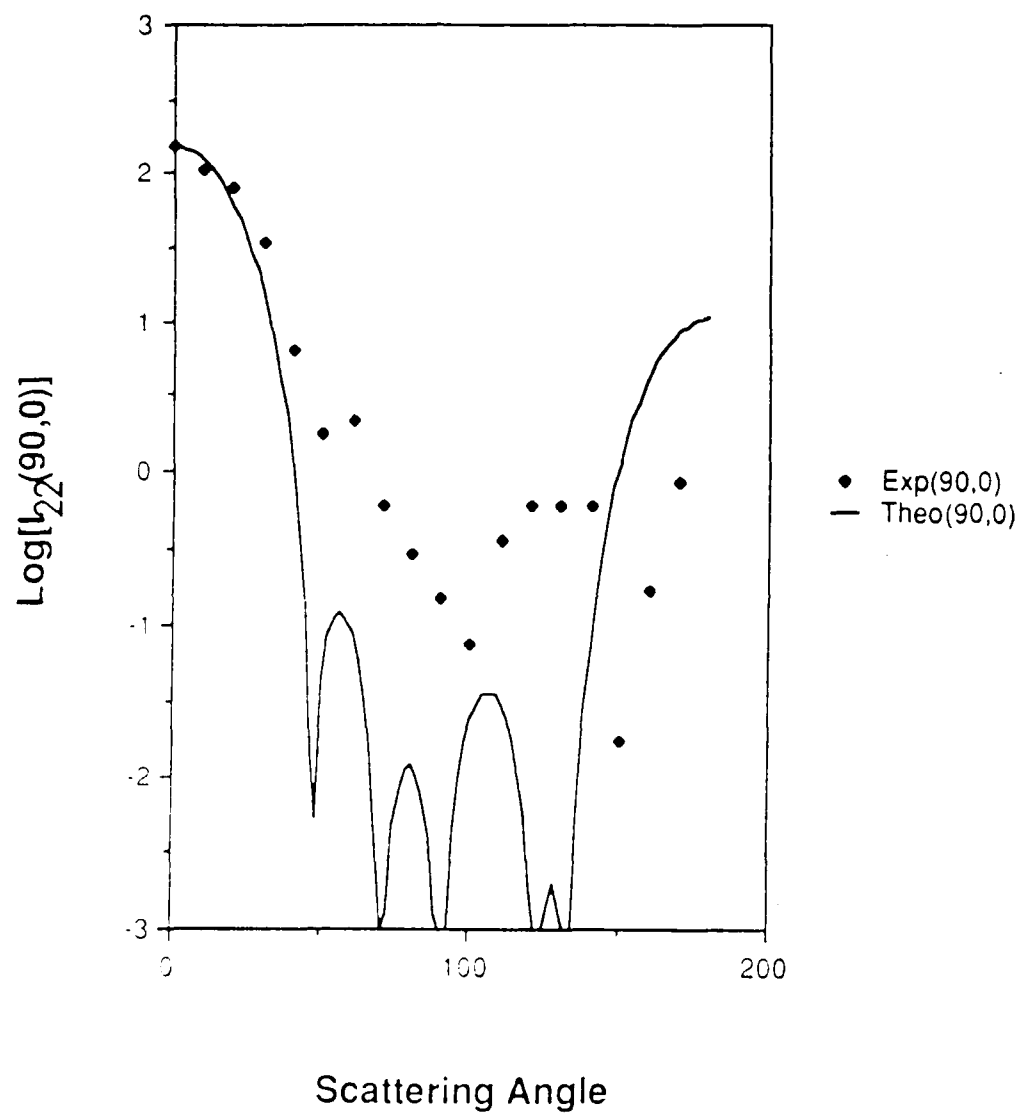
Figure 33. A comparison betwen theory and experiment for the log (I_{11}) plotted against the scattering angle 2 ϕ_0 for the orientation $\phi_t = 90$ and $\gamma_t = 0$.

Figure 34. A comparison betwen theory and experiment for the log (I_{22}) plotted against the scattering angle 2 θ_0 for the orientation $\phi_t = 90$ and $\gamma_t = 0$.
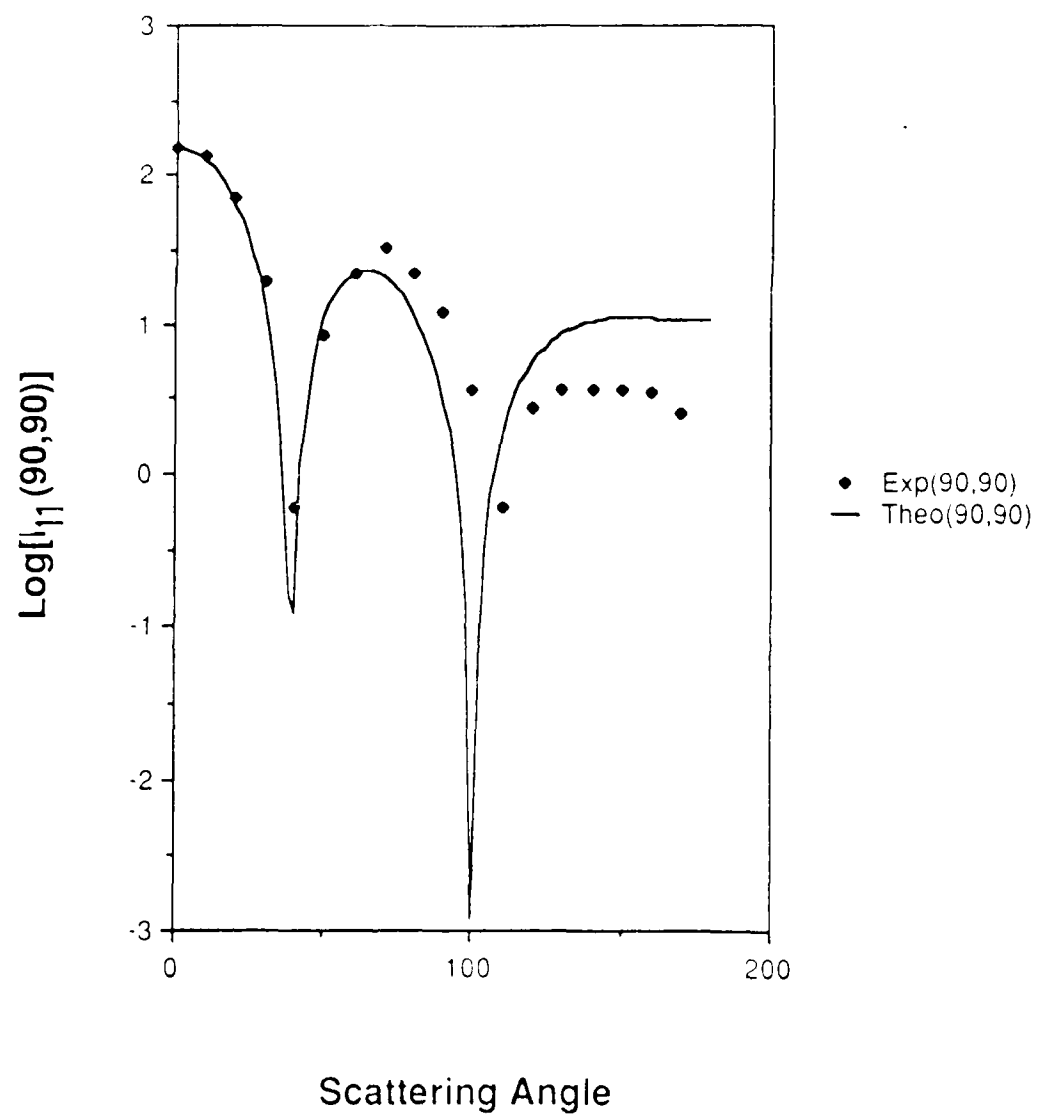
Figure 35. A comparison between theory and experiment for the log (I_{11}) plotted against the scattering angle 2 θ_0 for the orientation $\theta_t = 90$ and $\gamma_t = 90$.
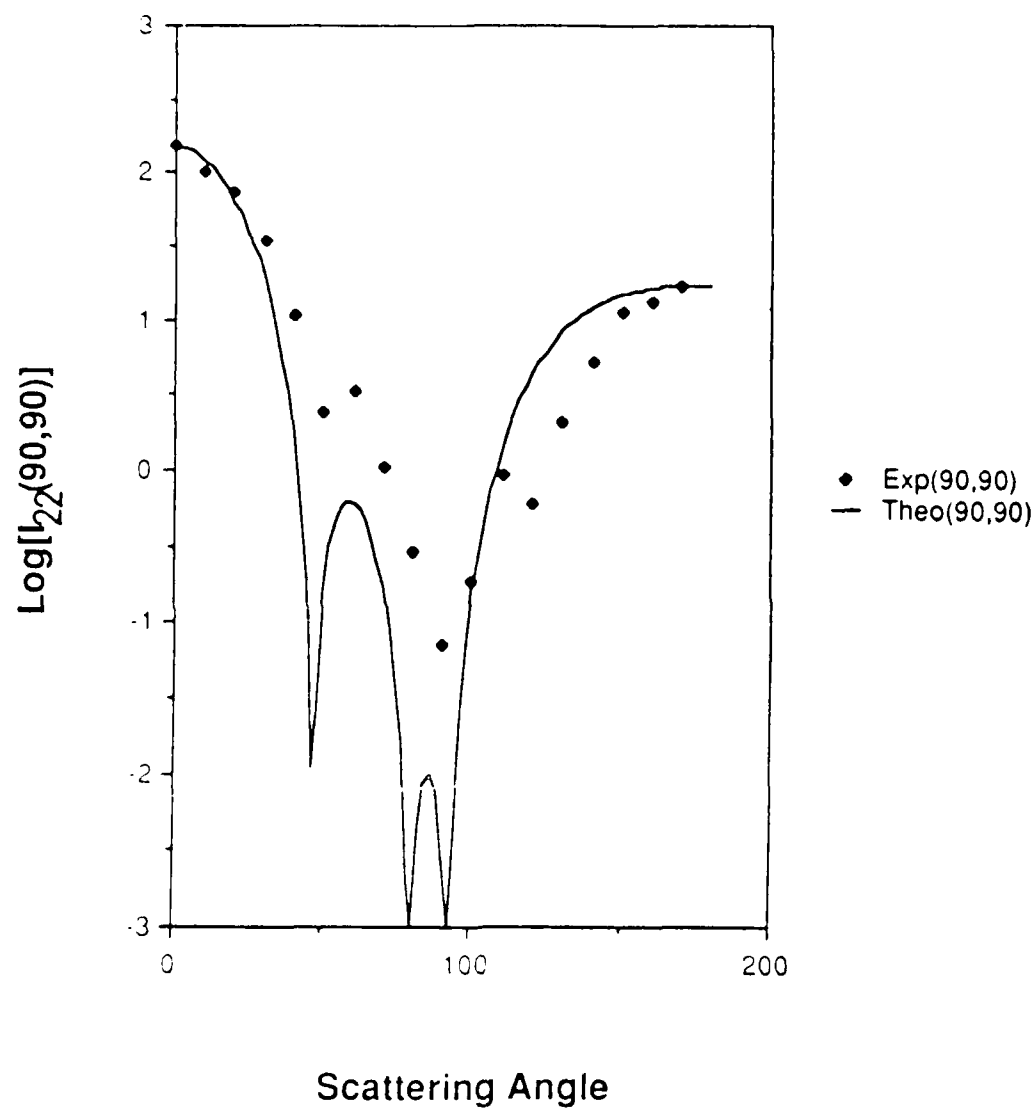
Figure 36. A comparison of the theory and experiment for the log (I_{22}) plotted against the scattering angle $2\,\theta_0$ for the orientation $\theta_t = 90$ and $\gamma_t = 90$.

REFERENCES

1. L.D. Cohen, R.D. Haracz, A. Cohen, and C. Acquista, Appl. Opt. 23, 742 1983.

2. A. Cohen, L.D. Cohen, R.D. Haracz, V. Tamaselli, J. Colosi, and K.D. Moeller. J. Appl. Phys. 56, 1329(1984)

3. A. Cohen. Opt. Letters 5, 150(1980).

4. A. Cohen, L.D. Cohen, R.D. Haracz, and S. Egert. J. Appl. Phys. 57, 698(1985).

5. A. Cohen, R.D. Haracz, and L.D. Cohen. J. Appl. Phys. 58,1135(1985).

6. R.D. Haracz, L.D. Cohen, A. Cohen, J. Appl. Phys. 58, 3322(1985)

7. M. Kerker, The scattering of Light and Other Electromagnetic Radiation, Academic press, New York, 1969.

8. N.L. McKay, T. Timusk, and B Farnsworth, J. Appl. Phys. 55, 4064(1984)

9. J.J. Stephens, J. Atmos. Sci. 37, 435(1980)

10. P. Huffman and W.R. Thursby, J. Atmos. Sci 26, 1073(1969))

11. K.S. Shifrin, Scattering of Light in a Turbid Medium (Moscow, 1951; published by NASA TTF-477, Washington, D.C., 1968)

12. C. Acquista, Appl. Opt. 15, 2932 (1976).

13. R.D. Haracz, L.D. Cohen, and A. Cohen, Appl. Opt. 23, 436(1984).

14. S. Asano and G. Yamamoto, Appl. Opt. 14, 29 (1975).

15. S. Zeitz, A. Belmont, and C. Nicolini, Cell Biophysics 5, 163 (1983).

16. C. Bustamente, M. Maestre, and I Tinoco, Jr., J. Chem. Phys. 73, 4272 (1980)

17. C. Bustamente, M. Maestre, and I. Tinoco, Jr., J. Chem. Phys. 73, 6046 (1980).

18. C. Bustemente, and M. Maestre, J. Chem. Phys. 74, 4839 (1981).

19. S.B.Singham,C.W.Patterson, and G.C.Saltzman, J. Chem Phys. 85(2),15(1986).

END

DATE

FILMED

DTIC

4/88